

Washington University in St. Louis

## Washington University Open Scholarship

---

Arts & Sciences Electronic Theses and  
Dissertations

Arts & Sciences

---

8-24-2023

### Effect of Age at Injury on Neuroinflammatory Response, Microstructural Outcomes, and Function Following Traumatic Brain Injury

Sydney J. Oswalt Reitz  
*Washington University in St. Louis*

Follow this and additional works at: [https://openscholarship.wustl.edu/art\\_sci\\_etds](https://openscholarship.wustl.edu/art_sci_etds)



Part of the [Neurosciences Commons](#)

---

#### Recommended Citation

Oswalt Reitz, Sydney J., "Effect of Age at Injury on Neuroinflammatory Response, Microstructural Outcomes, and Function Following Traumatic Brain Injury" (2023). *Arts & Sciences Electronic Theses and Dissertations*. 3133.

[https://openscholarship.wustl.edu/art\\_sci\\_etds/3133](https://openscholarship.wustl.edu/art_sci_etds/3133)

This Dissertation is brought to you for free and open access by the Arts & Sciences at Washington University Open Scholarship. It has been accepted for inclusion in Arts & Sciences Electronic Theses and Dissertations by an authorized administrator of Washington University Open Scholarship. For more information, please contact [digital@wumail.wustl.edu](mailto:digital@wumail.wustl.edu).

WASHINGTON UNIVERSITY IN ST. LOUIS

Division of Biology and Biomedical Sciences  
Neurosciences

Dissertation Examination Committee:

Terrance Kummer, Chair

John Cirrito

Stuart Friess

Celeste Karch

Tristan Li

Effect of Age at Injury on Neuroinflammatory Response, Microstructural Outcomes, and  
Function Following Traumatic Brain Injury

by

Sydney Oswald Reitz

A dissertation presented to  
Washington University in St. Louis  
in partial fulfillment of the  
requirements for the degree  
of Doctor of Philosophy

August 2023  
St. Louis, Missouri

© 2023, Sydney Oswalt Reitz

# Table of Contents

List of Figures.....	v
List of Tables .....	vi
Acknowledgments.....	vii
Abstract.....	ix
Chapter 1: Introduction.....	1
1.1 Traumatic Brain Injury .....	1
1.1.1 Intro to TBI.....	1
1.1.2 TBI as a Multiphasic Injury .....	1
1.2 Capturing TBI Pathology .....	2
1.2.1 Overview.....	2
1.3 TBI in the Aged Brain .....	3
1.3.1 Introduction to TBI in the Aged Brain.....	3
1.3.2 Synapses as a Target of Outcome Disparity .....	3
1.3.3 Neuroinflammation in the Aged Brain .....	4
Chapter 2: SEQUIN: An Imaging and Analysis Platform for Quantification and Characterization of Synaptic Structures in Mammalian Neuropil .....	5
2.1 Introduction to SEQUIN .....	5
2.2 Methods .....	5
2.2.1 Before You Begin.....	5
2.2.2 Immunofluorescent Labeling .....	10
2.2.3 Image Acquisition .....	15
2.2.5 Puncta Detection.....	22
2.2.6 Pre-to-Postsynaptic Puncta Separation Analysis.....	26
2.2.7 Data Representation (Optional) .....	27
2.3 Expected Outcome.....	27
2.4 Quantifications and Statistical Analysis .....	28
2.5 Limitations .....	30

2.6	Troubleshooting.....	30
2.7	Conclusions and future directions.....	35
Chapter 3: Enhanced Multiplexing of Immunofluorescence Microscopy Using a Long-Stokes-Shift Fluorophore.....		36
3.1	Introduction and Background Information.....	36
3.2	Strategic Planning.....	39
3.3	Methods.....	42
3.3.1	Basic Protocol 1: Four-Probe Immunofluorescence Labeling.....	42
3.3.2	Basic Protocol 2: Four-Probe Immunofluorescence Imaging.....	52
3.4	Critical Parameters.....	55
3.5	Troubleshooting.....	59
3.6	Understanding Results.....	60
3.7	Conclusions.....	61
Chapter 4: TBI in the Aged Brain.....		64
4.1	Introduction to TBI in the Aged Brain.....	64
4.2	Methods.....	64
4.2.1	Animals.....	64
4.2.2	Traumatic Brain Injury.....	65
4.2.3	Behavior.....	66
4.2.4	Tissue Collection.....	68
4.2.5	Immunohistochemistry.....	68
4.2.6	Image Collection.....	69
4.2.7	Image Processing and Analysis.....	70
4.2.8	Cellular Proliferation Assay.....	71
4.2.9	Statistics.....	72
4.3	Results.....	72
4.3.1	Excitatory Synaptic Density.....	72
4.3.2	CA1 Neuron Loss.....	74
4.3.3	Microglial Density and Proliferation.....	75

4.3.4	Synaptic Phagocytosis by Microglia.....	<b>77</b>
4.3.5	Functional Outcomes.....	<b>80</b>
4.4	Discussion.....	<b>83</b>
Chapter 5: Conclusion and Future Directions.....		<b>87</b>
5.1	Conclusions.....	<b>87</b>
5.1.1	Microstructural changes following TBI in the adult and aged mouse brain.....	<b>88</b>
5.1.1.1	Synapse loss following TBI .....	<b>88</b>
5.1.1.2	Neuron loss following TBI.....	<b>89</b>
5.1.2	Neuroinflammatory profile changes following TBI in the adult and aged mouse brain	<b>90</b>
5.1.3	Functional changes following TBI in the adult and aged brain .....	<b>93</b>
5.1.4	Summary .....	<b>94</b>
5.2	Future Directions .....	<b>94</b>
References.....		<b>97</b>

# List of Figures

Figure 2.1: Image Preprocessing.....	22
Figure 2.2: Puncta Detection in Tissue.....	25
Figure 2.3: Synaptic Quantification Strategy.....	28
Figure 2.4: Additional Synaptic Quantification Strategies.....	30
Figure 2.5: Minimal-to-no Synapse Peak.....	31
Figure 2.6: Left Shifted Frequency Distribution.....	32
Figure 2.7: XY Shift.....	33
Figure 2.8: Fluorescence intensity variation through Z.....	34
Figure 3.1: Excitation and emission spectra of Alexa Fluor 488 and ATTO 490LS.....	38
Figure 3.2: Image of mouse cortex co-labeled against CD68, synapsin 1/2, Iba1, and GFAP....	42
Figure 3.3: Laser lines and choice of emission filters for imaging each fluorophore without spectral cross-talk.....	58
Figure 3.4: No-primary controls revealing no spectral cross-talk or non-specific labeling.....	61
Figure 4.1. TBI causes hippocampal excitatory synapse loss in both adult and aged animals.....	73
Figure 4.2. TBI and age effects on CA1 nuclear band thickness.....	75
Figure 4.3. TBI increases microglial number and enhances proliferation.....	77
Figure 4.4. TBI increases CD68+ volume.....	79
Figure 4.5. Minimal age-dependent effects on functional endpoints after TBI.....	82

# **List of Tables**

Table 2.1: Sequin Key Resources Table.....	9
Table 2.2: List of Immunolabeling and Imaging Controls.....	10
Table 3.1: Controls.....	41

# **Acknowledgments**

Thank you to my thesis advisor, Terrance Kummer, my laboratory mentor Andrew Sauerbeck, all additional members of the Kummer lab 2017-2023. Additionally, I'd like to thank the four members of my thesis committee, John Cirrito (chair), Stuart Friess, Celeste Karch, and Dr. Tristan Li. Finally, I'd like to thank Marta Celorrio-Navarro for sharing her expertise in mouse models of brain injury with me, and Lindsay Laws, for her contribution to the genesis of this project.

This work was supported by the BrightFocus and Brain Research Foundation, the McDonnell Center for Cellular and Molecular Neurobiology, the National Institutes of Health, and the United States Department of Veterans Affairs.

Sydney Oswald Reitz

*Washington University in St. Louis*

*August 2023*

Dedicated to my parents.

## ABSTRACT OF THE DISSERTATION

Effect of Age at Injury on Neuroinflammatory Response, Microstructural Outcomes, and

Function Following Traumatic Brain Injury

by

Sydney Oswald Reitz

Doctor of Philosophy in Biology and Biomedical Sciences

Neurosciences

Washington University in St. Louis, August 2023

Professor Terrance Kummer, Chair

Traumatic brain injury (TBI) is a significant public health concern. Elderly individuals are more likely to be hospitalized and die from a TBI than younger victims, and experience worse outcomes along a series of clinical and functional endpoints. Studies exploring the mechanisms responsible for these outcome disparities are limited. As aging has been demonstrated to enhance baseline neuroinflammatory profile and is associated with synaptopathic neurodegenerative conditions linked to TBI, this thesis study sought to better characterize the relationship between aging-related neuroinflammation, microstructural—including synaptic—endpoints, and functional outcome following TBI. To this end, mice were subjected to diffuse and focal experimental brain injury at adult (3 months) and aged (18 months) time points. Microglial numbers and activity and hippocampal synapse and neuron loss were quantified along with learning and memory and anxiety-like behaviors at approximately one month post-injury. TBI impaired learning and memory and decreased hippocampal synaptic density in both age groups, but an effect of age was not detected. Aging similarly had no detectable, specific effect on hippocampal neuron loss in the setting of TBI, though older animals appeared to suffer greater

lesion size and disruption of hippocampus. TBI increased microglial density and proliferation, which was potentiated in aged animals. Microglial endosomal/lysosomal quantity and microglial phagocytosis of synaptic proteins were both increased by TBI, but there was no statistically-significant effect of age. These data support an enhanced cellular neuroinflammatory potential in aged animals following TBI, but minimal differences in specific structural or functional endpoints.

This thesis furthermore describes two novel immunofluorescence-based protocols developed in service of better understanding the role of TBI on synaptic health. The first protocol, SEQUIN, utilizes super-resolution microscopy to achieve synaptic resolution, enabling high throughput compared to related techniques. SEQUIN was used to quantify the density of excitatory synapses in the molecular layer of the CA1 region.

The second technique introduced an additional channel to standard immunofluorescence microscopy using a long Stokes-shifted fluorophore. This approach allowed for rigorous, quantitative, super-resolution imaging of four antigens in a single experiment. By utilizing this technique two synaptic proteins, microglia, and CD68 were all analyzed simultaneously, facilitating the study of synaptic phagocytosis.

# **Chapter 1: Introduction**

## **1.1 Traumatic Brain Injury**

### **1.1.1 Intro to TBI**

Traumatic brain injury (TBI), head injury caused by “blunt or penetrating trauma or from acceleration-deceleration forces,” is a major public health concern(Marr and Coronado, 2004).

TBI is the single most common cause of permanent disability in young people (under age 45) in Western countries, and accounted for nearly 224,000 hospitalization and 61,000 deaths in the U.S. in 2017 alone(Centers for Disease Control, 2021, 1999). Furthermore, in 2010, lifelong costs associated with traumatic brain injury, including both acute and ongoing costs of care, were estimated to be 77 billion dollars(Centers for Disease Control, 2019).

While the degree of disability is heterogenous and depends on severity and location of injury, common side effects of a moderate-to-severe TBI include short- and long-term memory loss, lesion-specific cognitive and motor impairment, and post-traumatic epilepsy(Annegers et al., 1998; Annegers and Coan, 2000; Masel and DeWitt, 2010).

### **1.1.2 TBI as a Multiphasic Injury**

It should be noted that TBI is a multiphasic injury. Primary injury is composed of tissue damage caused by the initial physical force, including but not limited to skull fracture, axonal shearing, and vascular damage. (Hammell and Henning, 2009; Mustafa and Alshboul, 2013; Vella et al., 2017). Secondary injury takes place in the hours to days following the primary injury, and encompasses sequelae of the initial injury, including edema, blood brain barrier breakdown, tissue hypoxia, etc. In the weeks following the injury, a more long-term (tertiary) phase of injury begins, characterized by unresolved neuroinflammation and neurodegeneration(Fleiss and

Gressens, 2012; Prasetyo, 2020). Primary injury can only be prevented (Mustafa and Alshboul, 2013; Vella et al., 2017). Secondary injury, the acute phase, has some limited interventions available to reduce injurious effects of primary injury such as cerebral edema (Friess et al., 2015; Vella et al., 2017). However, at less acute stages, not only are there no treatments available to prevent or ameliorate continued neuroinflammation and neurodegeneration, there is a general lack of understanding of the processes underlying this process and the relationship of neuroinflammation to outcome. Studying differential mechanisms of brain injury in the weeks to months following TBI will not only broaden the field's understanding of mechanisms of subsequent injury but also potentially offer translational targets to reduce neurodegenerative processes following traumatic brain injury.

## **1.2 Capturing TBI Pathology**

### **1.2.1 Overview**

Following TBI, a wide range of pathology can be found in the brain, including but not limited to contusions and lacerations, hemorrhage and hematoma, diffuse axonal injury, and increased gliosis (Mckee and Daneshvar, 2015). At the cellular level, neurons and synapses can be damaged and removed. However, discovery is often hindered by limited technology. To better understand these processes in the aged brain, new processes were developed and utilized. While these processes will be discussed at great lengths in later chapters, briefly *SEQUIN* (chapter 2) is a workflow designed to improve clarity and throughput of synaptic imaging, and Chapter 3 will detail use of an unusual fluorophore used to increase antigens that can be simultaneously quantified in a single section of tissue.

## **1.3 TBI in the Aged Brain**

### **1.3.1 Introduction to TBI in the Aged Brain**

While sport-related TBI in youth and young adults has merited and gained substantially greater public attention in recent years, the highest rates of TBI hospitalization and death occur in elderly individuals (Centers for Disease Control, 2021). In this population, fall-related TBIs are the most common cause of injury, with rates of fall-related deaths eight-fold higher for individuals 75 years and older than for individuals 55-74 (Peterson and Kegler, 2010). Not only are the elderly more likely to suffer a dangerous TBI, outcome is worse. Following a single TBI, individuals 60 years and older have higher rates of mortality, higher rates of post-traumatic epilepsy, and lower subsequent functional independence (Annegers et al., 1998; Annegers and Coan, 2000; Green et al., 2008; Hukkelhoven et al., 2003; Mosenthal et al., 2004; Stocchetti et al., 2012; Susman et al., 2002). Although these outcome disparities are well-documented, studies exploring the mechanisms responsible are limited.

### **1.3.2 Synapses as a Target of Outcome Disparity**

Recent literature has highlighted synapses as a particularly vulnerable target in aging-related neurodegenerative disease, with synapse loss exhibited in Alzheimer's disease (AD), Huntington's disease, Parkinson's disease, and Amyotrophic Lateral Sclerosis (ALS) (DeKosky and Scheff, 1990; Henstridge et al., 2016; Matuskey et al., 2020; Murmu et al., 2015; Selkoe, 2002; Terry et al., 1991). Furthermore, synapse loss is the best established pathological correlate of cognitive decline in AD, and manifests before other pathologies such as neuron loss (DeKosky and Scheff, 1990; Selkoe, 2002; Terry et al., 1991). It was recently demonstrated that excitatory synapse loss occurs following closed-head TBI in an animal model (Sauerbeck et al., 2020). This suggests the possibility of an interaction between trauma-induced synaptic injury and aging-

related processes in the brain, which may contribute to the structural-mechanistic linkages between TBI and AD.

### **1.3.3 Neuroinflammation in the Aged Brain**

Markers of CNS inflammation increase in healthy subjects across the lifespan. In aged human, canine, non-human primate, and rodent tissue, expression of Major Histocompatibility Complex II (MHCII), a marker of activated microglia, is upregulated as compared to adult controls (Perry et al., 1993; Rozovsky et al., 1998; Sheffield and Berman, 1998). Additionally, anti-inflammatory cytokine expression is suppressed as a result of aging (Sandhir et al., 2008). These effects are amplified in rodent models of TBI in aged animals compared to younger controls. Potentially as a result, aged animals have larger lesion volumes following TBI compared to adult controls (Kumar et al., 2013).

Neuroinflammatory processes are known to play key roles in the removal of synapses in aging as well as in AD and related neurodegenerative conditions (Hong et al., 2016; Shi et al., 2015). The role of these processes following TBI, and their potential modulation by age, however, has been underexplored. The study described in Chapter 4 addresses this question by assessing synaptic, microglial, and functional endpoints following experimental TBI in adult and aged mice.

# **Chapter 2: SEQUIN: An imaging and analysis platform for quantification and characterization of synaptic structures in mammalian neuropil**

## **2.1 Introduction to SEQUIN**

Synapses are crucial to normal brain function and frequent targets of disease, but current analysis methods cannot report on individual synaptic components in situ, or present other barriers to widespread adoption. For example, both array tomography and electron microscopy, both tools that reach synaptic resolution, are laborious and technically challenging, requiring specialty equipment to use. SEQUIN, Synaptic Evaluation and Quantification by Imaging Nanostructure, was developed to address this challenge. SEQUIN utilizes a widely available, accessible super-resolution platform in tandem with image processing and analysis to quantify synaptic loci over large regions of brain and characterize their molecular and nanostructural properties at the individual and population level. This protocol describes quantification of synaptic loci using SEQUIN.

## **2.2 Methods**

### **2.2.1 Before You Begin**

#### **Preparation of 30% Sucrose Buffer**

**Timing:** 15 minutes

30% sucrose in PBS with 0.02% sodium azide

1. For 1L, dissolve 300 g of sucrose in ~300 mL distilled water.

2. Add 100 mL of 10x PBS.
3. Adjust final volume to 1 L with distilled water.
4. Add 2 mL of 10% sodium azide to mixture.
5. Mix well before use.

**Caution: Sodium azide is toxic. Use appropriate personal protective equipment when preparing and using solution.**

### **Preparation of Cryoprotectant**

**Timing:** 15 minutes

30% ethylene glycol/30% sucrose in PBS

1. For 1 L, combine 300 mL ethylene glycol, 100 mL 10x PBS, and 200 mL distilled water.
2. Dissolve 300 g sucrose in solution.
3. Adjust final volume to 1 L with distilled water.
4. Mix well before use.

### **Tissue Preparation**

**Timing:** 3 days

1. Perfusion-fix tissue.
  - a. Anesthetize animals using 5% isoflurane.
  - b. Transcardially perfuse with ice cold PBS until the liver clears.
  - c. Switch to fresh ice cold 4% PFA in PBS pH 7.6 (made day of perfusion). Perfuse with PFA for 3 minutes. (NOTE: following successful perfusion, body will be very stiff, and vasculature will no longer be visible in brain.)

- d. Decapitate mouse and carefully extract brain.
  - e. Store in 20 mL 4% PFA overnight at 4° C.
2. Sucrose tissue.
    - a. Rinse tissue with 1x PBS.
    - b. Transfer to 20 mL 30% sucrose buffer.
    - c. Store in 30% sucrose buffer at 4° C at least 48 hours or until ready to section (ensure brain sinks to bottom of sucrose buffer before continuing).
  3. Section tissue.
    - a. Section tissue at 50 µm using a microtome and store in cryoprotectant buffer at -20°C until immunolabeling.

**Optional:** Labeling protocol below is described for free-floating tissue sections. 15 µm slide-mounted cryostat sections can be used with slight modifications.

### **Preparation of Blocking Buffer (20% Normal Goat Serum in 1x PBS)**

**Timing:** 15 minutes

1. Completely thaw and mix stock NGS.
2. Combine NGS and 1x PBS in a ratio of 1:4.
3. Vortex well.
4. Centrifuge mixture at 10,000-17,000xG for 5 minutes.
5. Avoid pellet when pipetting blocking buffer.

**Preparation of Antibody Buffer (10% Normal Goat Serum, 0.3% Triton X-100 in 1x PBS)**

**Timing:** 15 minutes

1. Completely thaw and mix stock NGS.
2. Combine NGS and 1x PBS in a ratio of 1:9.
3. Add Triton X-100 in a ratio of 3:1,000.
4. Vortex well.
5. Centrifuge mixture at 10,000-17,000xG for 5 min.
6. Avoid pellet when pipetting antibody buffer.

**Optional:** 10% NGS can also be attained by diluting blocking buffer 1:1 with 1x PBS and then adding Triton X-100.

REAGENT or RESOURCE	SOURCE	IDENTIFIER
<b>Antibodies</b>		
Rabbit anti-PSD-95 (1:200)	Invitrogen	Cat# 51-6900, RRID:AB_2533914
Guinea Pig anti-Synapsin 1/2 (1:500)	Synaptic Systems	Cat# 106004, RRID:AB_1106784
Mouse anti-Synapsin 1 (1:200)	Invitrogen	Cat# MA5-31919, RRID:AB_2787542
Goat anti-Rabbit IgG-Alexa 594 (1:200)	Invitrogen	Cat# A11037, RRID:AB_2534095
Goat anti-Guinea Pig IgG-Alexa 488 (1:200)	Invitrogen	Cat# A11073, RRID:AB_2534117
Goat anti-Mouse IgG-Alexa 488+ (1:200)	Invitrogen	Cat# A32723, RRID:AB_2633275
<b>Chemicals, Peptides, and Recombinant Proteins</b>		
10X Phosphate Buffered Saline	Corning	Cat# 46-013-CM
Normal Goat Serum	Vector	Cat# S-1000, RRID:AB_2336615
Mowiol 488	Electron Microscopy Services	Cat# 17977-150
Antifade 300	Electron Microscopy Services	Cat# 17977-25
1.5 H Coverglass	Marienfeld	Cat# 0107242
<b>Experimental Models: Organisms/Strains</b>		
Mouse: C57/BL6J	The Jackson Laboratory	Cat# 000664 RRID: IMSR_JAX:000664
<b>Software and Algorithms</b>		
Zen Digital Imaging for Light Microscopy	Zeiss	RRID:SCR_013672
Imaris	Bitplane	RRID:SCR_007370
MATLAB	MathWorks	RRID:SCR_001622
SEQUIN Matlab and Python Code	This report	<a href="https://github.com/KummerLab/SEQUIN">https://github.com/KummerLab/SEQUIN</a>
<b>Other</b>		
Zeiss LSM 880 Fast Airyscan	Zeiss	
Z Piezo	Zeiss	
63x Oil Objective	Zeiss	Cat# 420782-9900-000

**Table 2.1 SEQUIN Key Resources Table.**

## 2.2.2 Immunofluorescent Labeling

**Timing:** 2 days

Immunofluorescent labeling of synaptic proteins allows for visualization and identification of synaptic loci based on measured separation distances between pre- and postsynaptic markers.

This protocol demonstrates dual-antibody fluorescent labeling of 50  $\mu\text{m}$  free floating sections using antibodies against the presynaptic marker synapsin and the postsynaptic marker PSD-95.

Below we present two synapsin antibodies. Guinea pig anti-synapsin 1/2 is a convenient choice to avoid species cross-reactivity. However, due to lot-to-lot variability in this reagent mouse anti-synapsin 1 is a suitable option as well.

Necessary Controls	Function	Antibodies
No anti-PSD-95	To ensure secondary antibody specificity and lack of spectral crosstalk	1 <sup>0</sup> : Gp anti-Synapsin 1/2 OR Ms anti-Synapsin 1 2 <sup>0</sup> : Gt anti-Rb 594, Gt anti-Gp 488 OR Gt anti-Ms 488+
No anti-Synapsin		1 <sup>0</sup> : Rb anti-PSD-95 2 <sup>0</sup> : Gt anti-Rb 594, Gt anti-Gp 488 OR Gt anti-Ms 488+
Channel Alignment	To correct for chromatic aberration post-acquisition	1 <sup>0</sup> : Rb anti-PSD-95 2 <sup>0</sup> : Gt anti-Rb 594, Gt anti-Rb 488
Previously validated tissue* (optional)	To differentiate tissue preparation from immunolabeling problems	1 <sup>0</sup> : Rb anti-PSD-95, Gp anti-Synapsin 1/2 OR Ms anti-Synapsin 1 2 <sup>0</sup> : Gt anti-Rb 594, Gt anti-Gp 488 OR Gt anti-Ms 488+
Previously validated slide** (optional)	To confirm imaging and analysis workflow is performing as expected	

**Table 2.2. List of immunolabeling and imaging controls.**

\*Previously validated tissue is tissue that has previously been labeled, imaged, and analyzed and has yielded quantifiable results.

\*\* Previously validated slide is tissue that was previously labeled, imaged, and analyzed (using the same antibody combinations as the current experimental tissue) and yielded quantifiable results.

Abbreviations: Rb = Rabbit; PSD = Post-Synaptic Density; Gt = Goat; Gp = Guinea Pig; Ms = Mouse

- 1) Rinse sections three times in 1x PBS to remove cryoprotectant.
  - a) Fill 6 well plate with PBS (~12 mL/well) and add netwell inserts.
  - b) Fill 1L beaker with distilled water.
  - c) Using a clean paintbrush, carefully move sections to netwells.
  - d) Rinse on shaker at low speed for 5 minutes.
  - e) Fill another 6 well plate with PBS and move netwells from first plate to second.
  - f) Rinse on shaker at low speed for 5 minutes.
  - g) Repeat steps 1e and 1f for 3 washes total.
  
- 2) Block in 20% Normal Goat Serum (NGS) blocking buffer to prevent non-specific antibody binding.
  - a) Add blocking buffer to wells of a separate plate: ~500  $\mu$ L/well for a 24 well plate (up to 4 sections/well); ~750  $\mu$ L/well for a 12 well plate (up to 8 sections/well).
  - b) Using a clean paintbrush, carefully move sections from netwells with PBS to plates with blocking buffer.
  - c) Cover and incubate at RT on shaker at low speed for 1 hour.

- 3) Prepare primary antibodies while sections are incubating in blocking buffer.
  - a) Calculate the total volume of each antibody to be used and prepare “master-mixes” of each primary: ~500  $\mu\text{L}$ /well for a 24 well plate (up to 2 sections/well); ~750  $\mu\text{L}$ /well for a 12 well plate (up to 8 sections/well). Master-mixes are individual, 2x working dilutions (for labeling with 2 antibodies) of each.
  - b) Mix well.
  - c) Centrifuge mixture at 10,000-17,000xG for 5 min.
  - d) Avoid pellet when pipetting antibody.
  - e) antibody in antibody buffer that ensure equal distribution of antibody to each well. For >2 antibody labeling, master mixes will need to be further concentrated (*e.g.*, 3x for 3 antibodies).
  - f) Combine master-mixes to create final experimental, channel alignment control, and no-primary control antibody labeling solutions.
- 4) Incubate sections overnight with primary antibodies.
  - a) Using a paintbrush, carefully transfer tissue from blocking buffer plate to primary antibody plate. Ensure sections are submerged and mobile.
  - b) Fill empty wells with distilled water, cover.
  - c) Incubate overnight at room temperature.
- 5) Rinse three times in 1x PBS to remove unbound primary antibody by repeating step 1.

- 6) Prepare secondary antibodies.
  - a) Calculate total volume of each antibody mixture to be used: ~500  $\mu\text{L}$ /well for a 24 well plate (up to 2 sections/well); ~750  $\mu\text{L}$ /well for a 12 well plate (up to 8 sections/well).  
Creation of master-mixes is unnecessary for secondary antibodies.
  - b) Prepare fresh antibody buffer.
  - c) Add appropriate volumes of antibody to buffer.
  - d) Mix well.
  - e) Centrifuge mixture at 10,000-17,000xG for 5 min.
  - f) Avoid pellet when pipetting antibody.
- 7) Incubate sections in secondary antibody.
  - a) Plate secondary antibodies.
  - b) Transfer tissue from PBS to secondary antibody. Ensure sections are submerged and able to move freely.
  - c) Incubate on shaker at slow speed for 4 hours. Continue to steps 8 and 9 while incubating.
- 8) Prepare mounting media.
  - a) Calculate total volume required (150  $\mu\text{L}$ /slide).
  - b) Mix AF300 and MWL-488 in 1:9 ratio.
  - c) Vortex well.

- d) Centrifuge until bubbles are gone.
- 9) Clean 1.5H coverslips. Note: It is paramount that coverslips are spotless.
  - 10) After incubation in secondary antibodies, rinse sections three times in 1x PBS per step 1
  - 11) Mount tissue and coverslip.
    - a) Mount free-floating sections in 1x PBS.
    - b) Allow to dry in flat, dark location.
    - c) Immediately after tissue has completely dried and is adherent to the slide (~5-10 minutes), dunk slide in distilled water 5x quickly to remove salt residue.
    - d) Allow to dry again in dark, flat location (~2-10 minutes).
    - e) Apply 150  $\mu$ L mountant prepared above per slide by distributing among each section on the slide. Larger mountant volumes can be used if working with large numbers of sections (eight or more).
    - f) Slowly apply coverslip to avoid bubbles and apply gentle pressure to expel excess mountant.
    - g) Store in dark, flat place at room temperature for MWL to cure (at least 3 and ideally 7 days after coverslipping), allowing for maximal curing and for refractive index to increase and stabilize.

**Optional:** Between steps 9 and 10, DAPI may be applied to visualize nuclei. To do so, rinse sections once for 5 minutes in PBS, incubate in 1:50,000 DAPI in PBS in the same volume used for primary and secondary antibodies for 10-15 minutes, and then return sections to netwells and continue with step 10.

**Optional:** label with other/alternate markers (for primary synaptic analysis or subset analysis).

**Optional:** While above protocol is designed for free-float microtome-cut sections, a modified version of this protocol is also effective using 15  $\mu\text{m}$  cryostat-cut sections. For this variation, tissue is mounted on slides prior to immunolabeling.

**CRITICAL:** Protect secondary antibodies from light during and after labeling to avoid photobleaching.

**CRITICAL:** Create primary antibody master-mixes to avoid differing antibody concentrations in final labeling solutions due to pipetting error.

### 2.2.3 Image Acquisition

**Timing:** 10 min to set up, 2 min for each image acquired (acquisition can be automated)

The below protocol describes a typical acquisition suitable for SEQUIN analysis. Other parameters may suffice or be necessary for certain experimental aims.

12) Set up microscope.

- a) Turn on Zeiss LSM880 Fast Airyscan.
- b) Turn on light source.
- c) Select 63x 1.4 NA oil objective on the microscope display.
- d) Clean objective with lens cleaner.

- e) Mount Z-Piezo, a slide holder allowing for greater precision in Z translation.
- f) Apply Zeiss 518F immersion oil to objective.

13) Configure software.

- a) Open the Zen Black software, click “start system.”
  - i) While software loads, ensure slide is clean. (Note: use distilled water and lens cleaner to clean the cover glass.)
  - ii) Insert slide in Z-Piezo and tighten knobs securing slide until finger-tight. Slide should be firmly immobilized. If performing long scans (i.e. overnight) slide should be first loosely placed in the piezo and then firmly secured with dental wax.
- b) Navigate to “Maintain” tab.
  - i) Confirm objective listed in the software matches objective shown in the freestanding microscope control box.
  - ii) In the “System Options” box, navigate to the “Hardware” tab and ensure “Extended Z-Piezo” is unchecked.
  - iii) Navigate to the Airyscan menu within this tab and ensure “Adjust in continuous scans” and “Weak or sparse samples” are checked and “Adjust in slow time series” is unchecked.

14) Set experimental parameters.

- a) Move to “Acquisitions” tab.
  - i) Choose “8-bit bidirectional”.
  - ii) Use a zoom of greater or equal to 1.8x to optimize post-image Airyscan processing.
  - iii) Choose “Line” scan mode.
  - iv) Design appropriate light paths to image fluorophores chosen.

- (a) For each light path, select the appropriate laser to be used.
- (b) Open pinhole to maximum size.
- (c) Set gain to 800.
- (d) Select appropriate filters and beam splitters.
- v) Click “Optimal” to set XY pixel resolution of all channels selected. Note that all channels being imaged should be selected before clicking “optimal.”

15) Navigate to region of interest (ROI) using epifluorescent light source and oculars (“Locate” tab in Zen Black).

16) Set up imaging Z-Stack.

- a) Ensure “Z-Stack” is enabled in the top left corner of the “Acquisitions” tab.
- b) In the “Z-stack” window, Check “Use Piezo.”
- c) Set Z-stack configuration to “First-Last” mode.
- d) Select one of the laser channels and click “Live” in the top left panel of the “Acquisitions” tab.
- e) Using Z-Piezo control knob, find the cut edge of the tissue at the coverglass. (NOTE: it may help to “Best fit” the display parameters to visualize signal.)
- f) Find the first Z position that avoids irregularity at the cut surface and choose “set first” in the Z-stack control windows
- g) Rotate the piezo focus control to find the deepest tissue section that avoids surface irregularity and select “set last.”
- h) Navigate to the center of the stack (click “c” on the Z stack diagram in the “Z-stack” window).

- i) Within the Z stack window, set the step size (“Interval”) to 120 nm and number of optical sections (“Slices”) to 35. Note that other stack thicknesses (number of optical sections) may be appropriate for a given experiment.
- j) Scroll through the entirety of the now shorter stack (4.08  $\mu\text{m}$  centered in the section) and ensure suitability of all optical sections.
- k) Turn off “Live” mode.

17) Align Airyscan detector.

- a) Turn on “Continuous mode”.
- b) While continuous mode is running, open the Airyscan view on the display window. A display of the 32 detectors is depicted. The brightest detector should be the central element. If not, give the scope several moments to autoadjust. Do not proceed until the brightest detector is centered.

18) Set up laser ramping.

- a) Check the “Z-correction” box in the Z-stack window.
- b) Select the first channel to laser ramp for and start “Continuous” mode.
- c) Move to the deepest position of the Z-stack.
- d) Change the laser intensity of the selected channel until the lower 1/3 of the dynamic range of pixel intensity is occupied, as represented by the histogram in the “Display” tab.
- e) Move to the first position in the Z-stack and find the laser intensity that best replicates the signal acquired at the deepest position.
- f) Repeat this for all channels.

g) When desired laser ramp is set for all channels, move back to the most superficial position, select all channels, and enter the laser intensity for the first position for each.

Then, click “Add position” in the Z-stack window.

h) Move to the last position and repeat.

19) Ensure acquisition speed is set to maximum.

20) Now, select “begin experiment” to begin the scan (duration is approximately 2 minutes for above parameters).

21) When image acquisition is complete, save image. Before proceeding with further imaging, Airyscan process the image (see Image Processing below) and check the orthogonal view to ensure consistent Z intensity (see Troubleshooting). If brightness is not consistent, move to a different field and reset the laser ramp.

**Optional:** Zoom can be varied to any value greater than 1.8x.

**Optional:** While this protocol discusses imaging synaptic markers that emit in the green and red portions of the spectrum, SEQUIN can be completed with alternate or additional fluorophores.

However, settings for lasers, filter sets, and scanning mode must be adjusted.

**Optional:** Using microscope settings not discussed in this protocol, large automated scans can be set up to cover many contiguous or non-contiguous ROIs, as described in Sauerbeck et al., 2020.

## 2.2.4 Image Pre-Processing

**Timing:** 1-2 minute/image (can be largely automated)

Airyscan processing and channel alignment entail hardware-enabled deconvolution to improve signal-to-noise ratio (Airyscan processing) and pixel reassignment to correct for chromatic aberration (channel alignment) (Figure 2.1).

## 22) Airyscan Processing.

- a) Select “Processing” tab within Zen Black and choose “Airyscan Process” from dropdown menu.
- b) With the image of interest open, choose “Select Image.”
- c) Set Airyscan strength to 6.
- d) Choose “3D” option.
- e) Click “Apply.”
- f) Save new image as CZI.

## 23) Channel Align Airyscan Processed images (Figure 2.1).

- a) Find channel alignment value
  - i) Select “Processing” tab within Zen Black.
  - ii) Choose “Channel Align” from dropdown menu in left sidebar.
  - iii) Open previously acquired and Airyscan Processed channel alignment image and choose “Select Image” in the left sidebar.
  - iv) Unselect “Fit.”
  - v) Offset one channel in Y such that channels are no longer overlapping to facilitate visualization of chromatic aberration.
  - vi) Click “Apply” to create a new image.
  - vii) View the orthogonal projection of this image and focus on one dual-labeled puncta. Manually shift the Z value for one of the channels until the channel images are fully aligned. Record the Z value offset.
  - viii) Once image has been aligned, confirm suitability of adjustment value on multiple puncta throughout the image.

- ix) While XY correction is generally unnecessary when using the recommended 63x oil objective, less well-compensated objectives may require XY channel alignment.
- b) Channel align experimental images.
  - i) While in “Processing” tab, choose “Channel Alignment” and open and select experimental image to be channel aligned.
  - ii) Unselect “Fit.”
  - iii) Input the recorded Z offset and save the new CZI.

**Optional:** Airyscan processing can be batched. To do so, click “Run Batch” in the bottom of the window and select the files to be processed. Ensure “Auto” is unselected, strength is set to 6.0, and “3D” is selected.

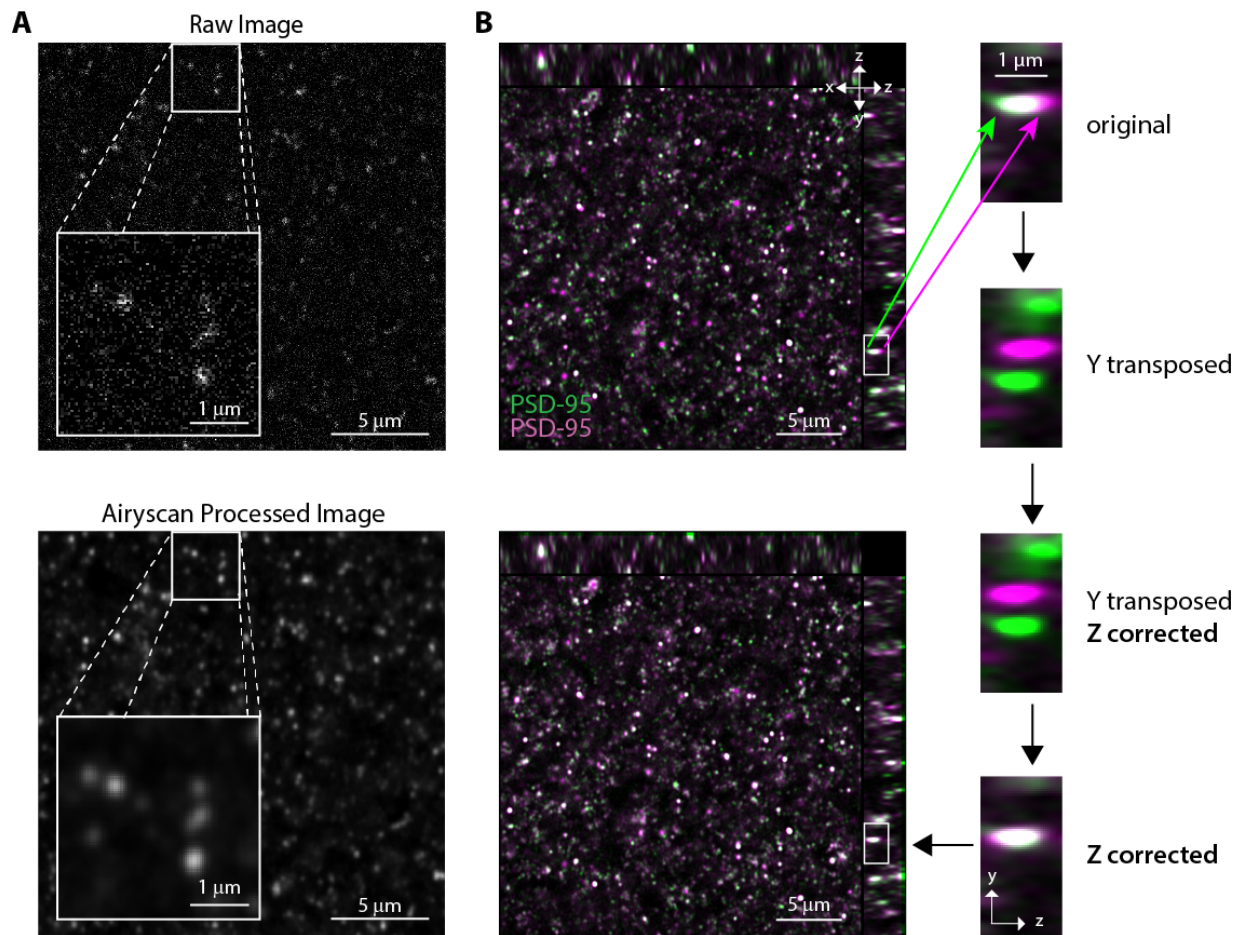


**Figure 2.1. Image preprocessing.** (A) Single detector (central detector) image prior to Airyscan Processing (above) and the Airyscan Processed result (below). (B) Channel Alignment image shown with orthogonal views before (upper left) and after (lower left) adjustment. Panels to right depict process for determining and correcting chromatic aberration in Z, involving a temporary transposition in Y.

## 2.2.5 Puncta Detection

**Timing:** 1-2 minute/image (can be largely automated)

Using Imaris, puncta are detected in the three-dimensional Airyscan processed, channel-aligned image. This will yield X, Y, and Z coordinates of the centroid of each puncta as well as metadata such as average intensity of each punctum. Although a minimal amount of coding experience is required, we have developed Python code that accomplishes the tasks below if Imaris is unavailable. This is available on Github (see Key Resources Table).

24) Place all Airyscan Processed and Channel Aligned images in a single folder.

a) Note all images must have the same Z dimensions.

25) Select images in Imaris (below steps describe spot creation using Imaris v9.5, but other versions are suitable with minor adaptations).

a) Open Imaris.

b) Click “Observe Folder” and navigate to folder of CZI images.

c) Choose “Select Folder”; folder will be added to list of “Observed Folders”.

d) Open folder in Imaris (double-click).

e) Select all images in the folder, right click, and select “convert to IMS”.

26) Create spots (Figure 2.2).

a) Select “New Batch” in top menu.

b) When a preview of the image appears, select “Next” to begin object creation.

c) To create spots, click “Spots” button. Create spots for each channel for analysis.

d) Set parameters for channel, size, and boundaries of spot creation in the “Create” window.

i) “Algorithm Settings”: leave all unchecked. Advance to next screen.

ii) “Source Channel”: choose the source channel for spots detection.

iii) Under “Spot Detection” (same screen)

(1) Check “Model PSF-elongation” along Z-axis and “Background Subtraction”.

(2) “Estimated XY Diameter” for punctum is generally set to 0.2  $\mu\text{M}$ .

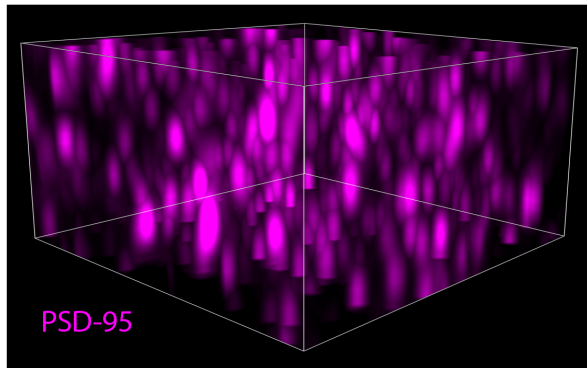
(3) “Estimated Z Diameter” for punctum is generally set to 0.6  $\mu\text{M}$ .

(4) Navigate to the next screen.

iv) “Classify Spots”: perform edge filtering (exclude spots not entirely contained within image boundaries).

- (1) Create two filters by clicking the plus sign twice.
  - (2) Highlight one filter and change it to “Distance to Image Border XY Img=1”  
above automatic threshold.
    - (a) Set the leftmost value of this filter to 0.1  $\mu\text{m}$  (half XY diameter from above)  
and ensure rightmost value is not activated.
  - (3) Change the second filter to “Position Z”.
    - (a) Set the left and right values so they are 0.3  $\mu\text{m}$  (half Z diameter from above)  
from the extremes. (ex: an image that ranged from 0.06 to 4.14 in Z would be  
filtered to between 0.36 to 3.84).
  - (4) Click the green arrow to complete the set-up process for this analysis.
    - v) Repeat Step 26 for all channels in need of puncta detection.
- 27) When all spots have been created and edited, choose the “OK” button in the Objects window.
- 28) Name the batch.
- 29) Right click the new batch and select “Run Batch” to run on all images in the folder. After the  
batch finishes, save as a CSV file.

Airyscan Processed Image



Spots Detected

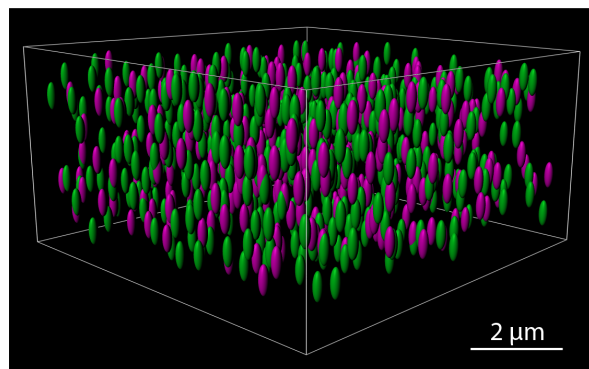
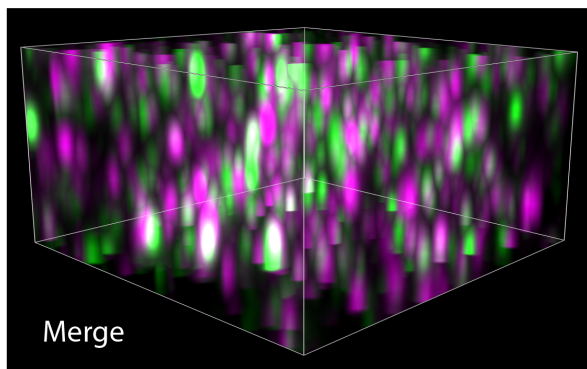
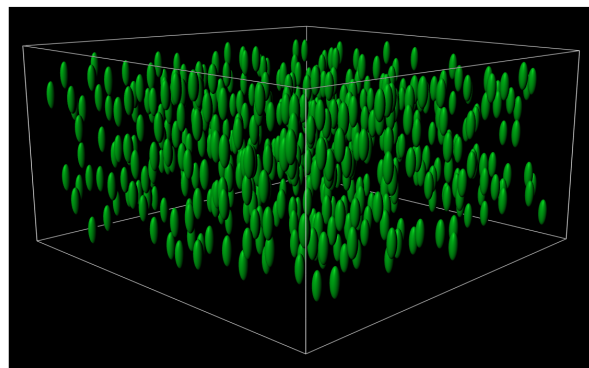
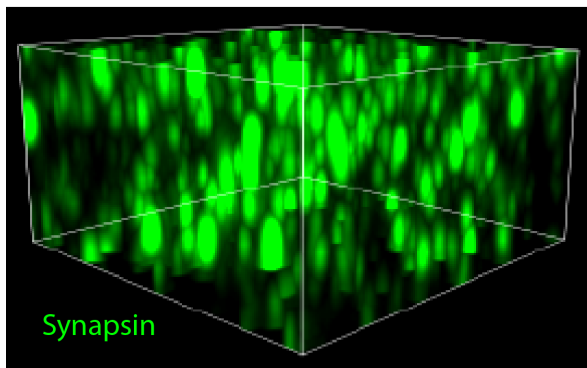
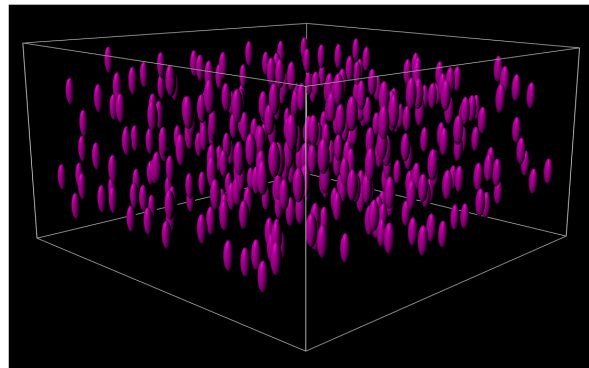


**Figure 2.2 Puncta detection in tissue.** Three dimensional image taken in mouse cortex labeled with PSD-95 and Synapsin. Enlarged panel shows puncta detection and rendering using Imaris, with appropriate filtering applied to remove puncta at the edges of the image.

## 2.2.6 Pre-to-Postsynaptic Puncta Separation Analysis

**Timing:** dependent on computational resources; < 1 minute/image (automated) on high-end workstations to several minutes per image

Using Matlab, Euclidian distances between pre- and postsynaptic puncta will be measured for each pre- or postsynaptic punctum in 3 dimensions, yielding raw as well as binned separation data (sorted by separation distance). One marker—can be pre- or postsynaptic—is used as the reference dataset, and the nearest neighbor from the other dataset will be matched to each puncta in the referenced dataset (NOTE: while either pre- or postsynaptic puncta can serve as the reference dataset, all examples shown use PSD-95). In many cases, only the top 20% brightest pre- and postsynaptic puncta are analyzed. Spots of lower intensity contain fewer puncta pairs consistent with synapses, though this is dependent on antibody and marker choice and should be experimentally determined (Sauerbeck et al., 2020). All referenced code is available on Github (see Table 2.1).

30) Confirm identity of spots in output folders.

- a) Caution! If spots are named during Batch creation, Imaris will output and save detected spots in alphabetical order and rename to “Spot\_1”, “Spot\_2”, “Spot\_3”, etc based upon order of output.
- b) Confirmation of exactly which spot type is in a given folder can be determined by viewing one of the output statistic files (i.e. Spots\_1\_Area) and looking in column H for the displayed spot name.
- c) Folders for each of the spots that were created can be renamed to match the marker of interest, if desired.

31) Analyze separation distances.

- a) Open Matlab.
- b) Edit the code to execute file to reflect all needed parameters.
  - i) The first spot listed as ‘Spot 1’ in Matlab will be used as the referenced dataset.
- c) Paste the code to execute into Matlab’s command window and press “enter.”

32) Compile image colocalization data into one workbook.

- a) When the analysis completes, compile all finished files (found in the newly created “data output” folder) using the “compile Excel docs” code.

### **2.2.7 Data Representation (Optional)**

**Timing:** 3 minutes

33) Retrieve generated pre-to-postsynaptic separation distances.

- a) The Nearest Neighbor code will create a “data output” folder where the input Imaris data was located. The “compile Excel docs” code will create a “compiled data” folder inside of “data output.”
- b) The tab “Normal Frequency” within the Excel doc will contain frequency distributions of images sorted into bins of 20 nm. Each column represents a different image.

34) Graph data.

- a) Plot the frequency distribution data found on the “Normal Frequency” tab in the Excel doc against a geometric series “10 nm, 30 nm, 50 nm, [...]”. This series represents the center of the histogram bins.

## **2.3 Expected Outcome**

When the technique is performed as described in healthy brain tissue, one expects to see a bimodal histogram of pre-to-postsynaptic separation distances. The first peak, typically found at

150-200 nm, represents pre-postsynaptic marker pairs separated by distances ultrastructurally consistent with synapses. The second peak, found at longer separation distances, represents non-synaptic associations in the volume (Figure 2.3). The area under the first peak (quantified as described below) corresponds to the quantity of synaptic loci within the imaged volume. In the setting of certain forms of acute injury (Sauerbeck et al., 2020), neurodegenerative processes (Sauerbeck et al., 2020; Terry et al., 1991; Gratuze et al., 2020) or other processes that reduce synapse number, the area under this peak is expected to be lower compared to controls.

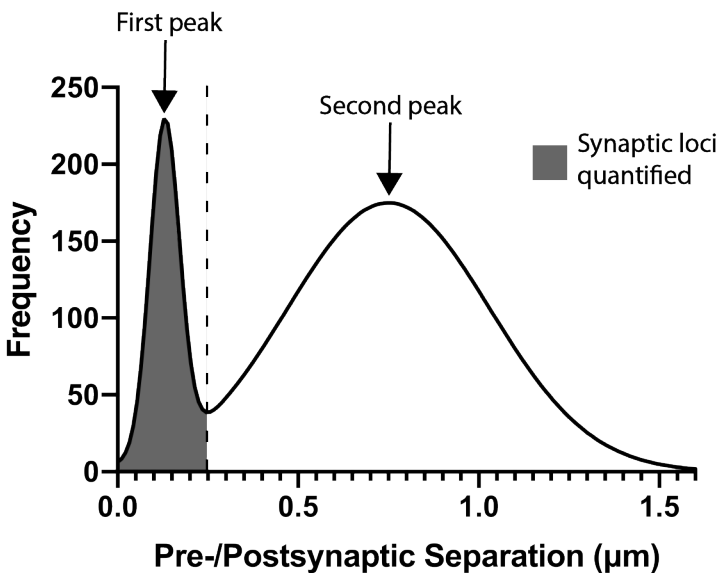


**Figure 2.3. Synaptic Quantification Strategy.** Bimodal histogram indicating both the first and second peaks. Dashed line marks cutoff point, and shaded region indicates area to sum for synaptic quantification (note other quantification options may be used; see text and Figure 2.4).

## 2.4 Quantifications and Statistical Analysis

To perform a basic quantification of synaptic loci, sum all puncta counts falling to the left of an experimentally-determined cut off (for example, < 250 nm pre-to-postsynaptic separation, or the trough between the first and second peak). Given variability between experimental models and conditions, this cutoff point may vary for different applications (Figure 2.3).

The early peak may be more completely ‘disentangled’ from the broad second peak by incorporating “flipped” data into the analysis, or modeling the pre-to-postsynaptic separation histogram as a mixture of two Gaussians (Figure 2.4). For the “flipped” analysis, spots data for one of the marker channels (pre- or postsynaptic) are first reflected across the Y axis and then the nearest neighbor analysis is undertaken with the paired, unaltered marker channel coordinates (e.g., the PSD-95 spots coordinates are reflected and a separation analysis is performed with unreflected synapsin spot coordinates). Plotting the flipped data should yield a unimodal distribution indicative only of random pairings. This data can be found in the generated spreadsheet in the tab “Flipped Frequency”. These random pairings can then be subtracted from the prior (unflipped) nearest neighbor analysis on a bin-wise basis. The results of this subtraction can be found in the sheet titled “Flip Subtraction Frequency”. Plotting the flip subtraction data should yield a sharp early peak with a minimal or negative second peak. Finally, the “Flip Sub Zeros Frequency” uses the same algorithm to remove random pairings as found in the “Flipped Frequency,” but subsequently zeroes any biologically-meaningless negative values.

2-Gaussian modeling can be performed with a number of graphing and analysis packages (Matlab, R, Graphpad Prism, etc.). In this case the first of the 2 resulting Gaussians represents paired puncta consistent with synaptic loci, while the second (at a longer separation distance) represents random pairings.

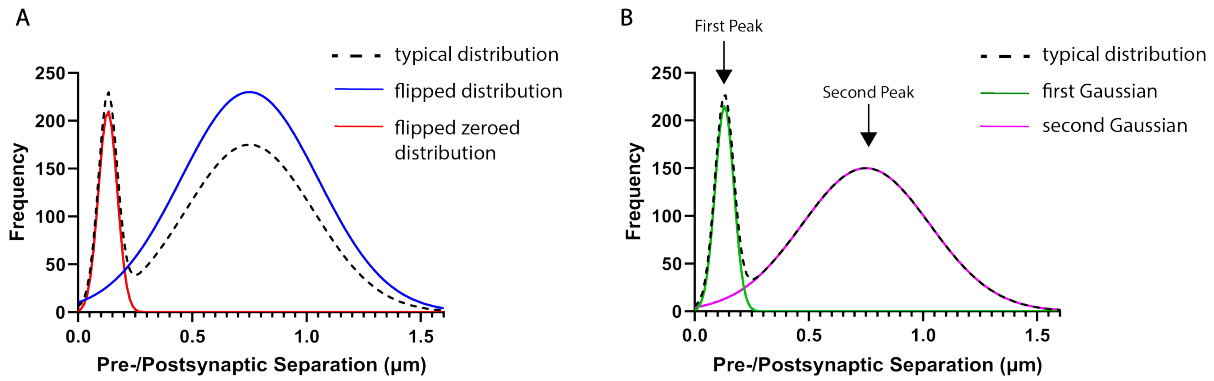


**Figure 2.4. Additional synaptic quantification strategies**

Standard frequency distribution, overlaid with flipped distribution and flip subtracted zeros distribution. (B) Gaussian curves fitted to the first and second peak of a standard frequency distribution.

## 2.5 Limitations

SEQUIN has only been validated in aldehyde-fixed tissue.

The quality of refractive index matching currently limits the depth of analyzable tissue. Currently the SEQUIN analysis becomes challenging to interpret at depths below 50 μm.

## 2.6 Troubleshooting

**Problem:** The synapse peak is minimal or indistinguishable from the noise peak (Figure 2.5).

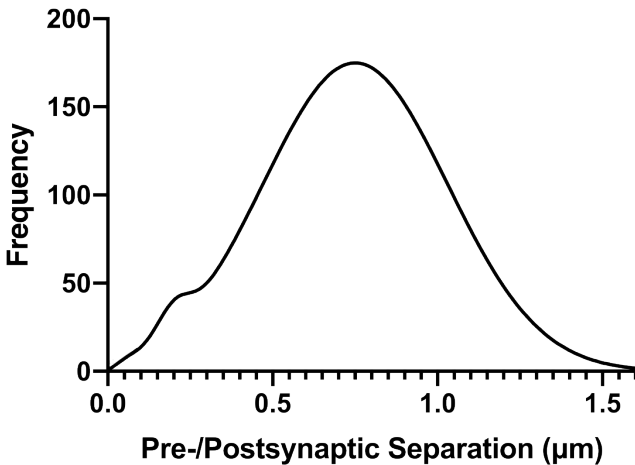


**Figure 2.5. Minimal-to-no synapse peak.** Frequency distribution with little-to-no synapse peak.

Potential Solution:

Lack of a typical bimodal frequency distribution of pre-to-postsynaptic separations with a clear early peak and broader following peak could be due to a variety of problems occurring in the tissue preparation, labeling and/or imaging steps. We present a strategy to isolate the problem.

Working backwards:

Quality check image analysis workflow: Repeat quantification on imaging data that has historically yielded expected results (or use sample data provided at <https://github.com/KummerLab/SEQUIN>) in tandem with experimental images. Repeat analysis of historical data should yield identical results.

Quality check imaging workflow: Compare previous and current quantification of the previously immunolabeled and validated sample (imaging validation sample; Table 2.1) that was imaged as a historical control. While quantification is not expected to be identical, an image from the same region using the same filter settings should yield a similar frequency distribution vs. historical data. Additional quality checks should include:

- Puncta brightness should be stable throughout the Z stack (assuming uniform distribution of markers).
- Image should be free of tissue artifacts or excessive autofluorescence.
- Z stack should be centered in tissue.

Quality check histological workflow: Examine no-primary controls to assess background levels and unexpected antibody cross-reactivity (primary or secondary). This protocol should yield very low background using the suggested fluorophores. Examine results of analysis of tissue control (Tissue validation control; Table 2.1) to rule out poor clearance or fixation of experimental tissue, or other potential problems with tissue harvesting and processing.

**Problem:** The frequency distribution is far-left shifted, with a small or nonexistent noise peak (Figure 2.6).

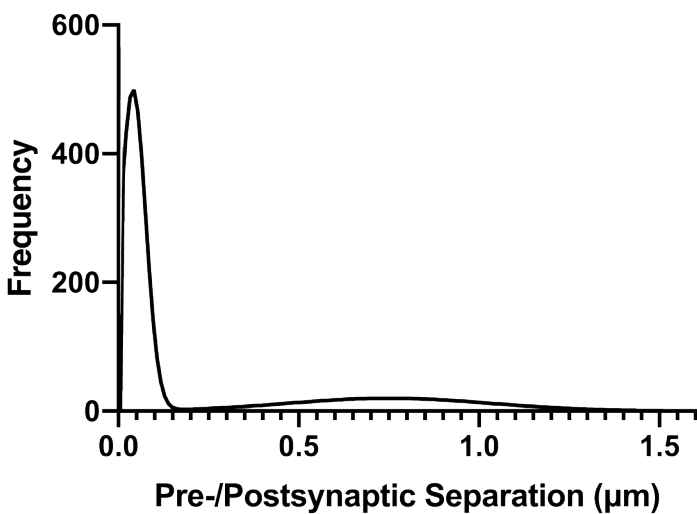


**Figure 2.6. Left shifted frequency distribution.** Left shifted frequency distribution with minimal secondary peak, often indicative of antibody or fluorophore cross-talk.

Potential Solution:

This can occur with antibody or fluorophore cross-talk. To identify the issue:

- Confirm correct filter sets were used to isolate target signal.
- Confirm antibody specificity using no-primary controls.
- Confirm correct immunolabeling techniques were implemented.

**Problem:** Puncta appear to “zigzag” through Z (Figure 2.7).

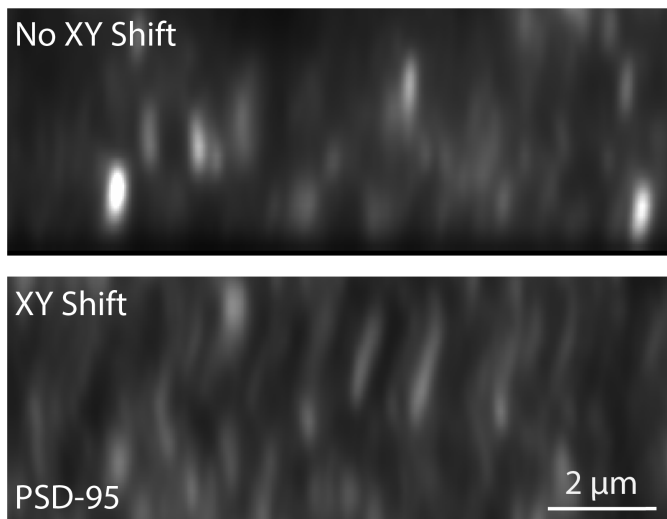


**Figure 2.7. XY shift.** An excerpt from an orthogonal view of an image from an imaging session in which the stage shifted during imaging (right panel) compared to an image from a session with minimal shift (left panel).

Potential Solution:

This indicates an XY shift of the stage during image acquisition. This can be an indication that the stage and/or slide are not properly secured or that the system was not given enough time to warm prior to the start of imaging (thermal shift). Ensure proper installation of both components and allow at least 30 min from the time the system is started until the first experimental images are acquired.

**Problem:** Fluorescence intensity is highly variable through Z, which causes faulty puncta detection (Figure 2.8).

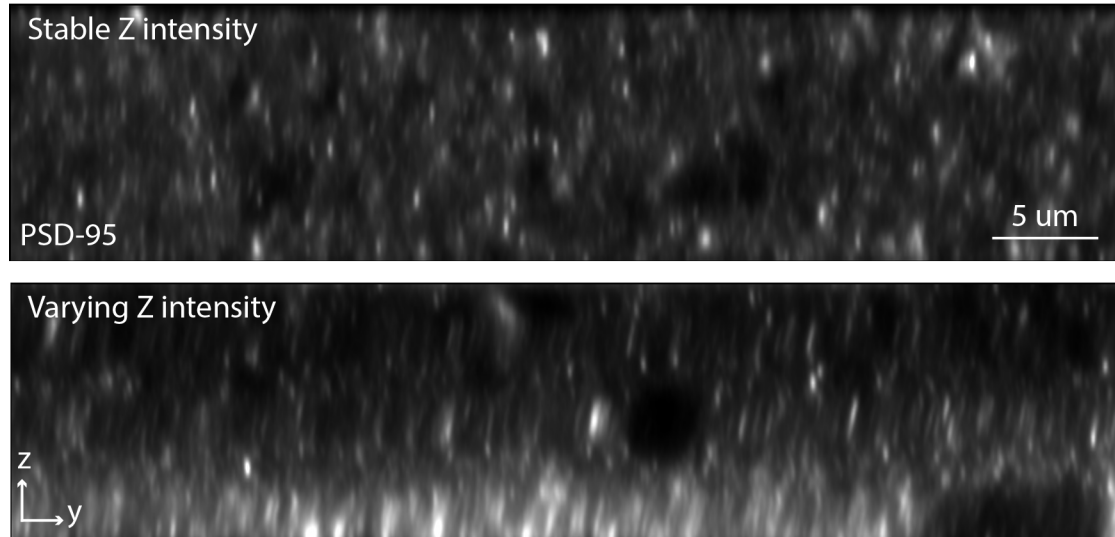


**Figure 2.8. Fluorescence intensity variation through Z.** An image with varying fluorescence intensity through Z (bottom) compared to an image with stable fluorescence intensity (top).

Potential Solution:

First confirm the Z-stack is centered in the middle of the tissue and neither the top nor the bottom are approaching the tissue cut surface. Tissue at the cut surface is occasionally more intensely labeled than tissue deeper within the section. Improper laser ramping is another possible cause.

## **2.7 Conclusions and future directions**

SEQUIN is a powerful tool that utilizes superresolution microscopy to change synaptic-resolution imaging from a laborious and technically-challenging process to a workflow relying on simple immunofluorescence and code. Using SEQUIN, synapses can be quickly quantified in volumes that would have previously taken years using electron microscopy or array tomography. While SEQUIN has been used to describe excitatory synaptic populations, future work could optimize SEQUIN for inhibitory subsets and use it as a tool to measure excitatory:inhibitory ratios in disease.

# **Chapter 3: Enhanced Multiplexing of Immunofluorescence Microscopy Using a Long-Stokes-Shift Fluorophore**

## **3.1 Introduction and Background Information**

Immunofluorescence (IF) is an invaluable tool to localize target antigens in biological tissues.

This technique permits visualization of biomolecules via the direct or indirect binding of a fluorescent probe, followed by imaging with a fluorescence microscope. Since its demonstration almost 80 years ago (Coons et al., 1942), the development of a deep catalogue of fluorescently-labeled probes, as well as the ubiquitous deployment of fluorescence microscopes, have made IF an extremely powerful and highly-accessible technique.

One of the most common and useful applications of IF involves determining the spatial relationship of antigens *in situ*, a technique that requires the multiplexing of fluorescent probes. A key limiting factor in the power of these characterizations, however, is the number of fluorescent labels that can be both imaged efficiently and well-separated from one another (spectrally distinguished).

The total number of such multiplexed probes in a given sample is often practically limited to three, roughly occupying the blue-green, red, and infrared bands of the electromagnetic spectrum. Additional multiplexing is generally limited to architectural contrast (*e.g.*, cytoskeletal, DNA), as opposed to targeting a specific biomolecule of experimental importance that may have moderate-to-low abundance or antigenicity. That is, additional multiplexing generally relies on biomolecules for which uniquely efficient probes exist (*e.g.*, nuclear contrast)

or of uncommonly high abundance (e.g., cytoskeletal antigens), or both, that overcome inherent imaging inefficiencies related to light sources, probes, or tissue autofluorescence.

A number of approaches exist to address this limitation. From the standpoint of imaging and analysis, spectral imaging with linear unmixing and related approaches make use of specialized but now widely available hardware and algorithmic image processing to determine the underlying components of overlapping emission patterns from biosamples (Zimmermann, 2005). These approaches, however, generally rely on assumptions regarding fluorophore reference emission spectra that may be sample- or instrument-specific, or may present multiple valid solutions to convolved spectra (McRae et al., 2019; Neher et al., 2009; Tsurui et al., 2000). From the standpoint of labels, probes such as quantum dots with narrower emission spectra vs. standard organic fluorophores (among other advantages) enhance spectral discrimination, but present challenges related to their physical and biological properties (large size and potential toxicity, among other application-specific issues) that have limited their application (Jaiswal and Simon, 2004; Resch-Genger et al., 2008; Wegner and Hildebrandt, 2015). Existing approaches thus leave room for an accessible, low-friction method to enhance multiplexing beyond the standard three probes.

This protocol demonstrates such a method: application of a long Stokes shift organic fluorophore. The Stokes shift in this context is the difference between the maxima of the absorption and emission spectra for a specific fluorophore (Figure 3.1). This difference is substantially greater for long Stokes shift vs. conventional fluorophores. As a result, standard emission filters can adequately distinguish signal arising from a conventional fluorophore from that arising from a fluorophore with completely overlapping excitation properties, but a longer Stokes shifted emission maximum (Figure 3.1), without resorting to unmixing algorithms. In

tandem with two other conventional probes, such an approach permits the labeling and analysis of four target antigens *in situ* (Basic Protocol 1; Figure 3.2), all via standard IF histological and imaging methods. The below protocol furthermore describes approaches to rigorously avoid both spectral bleed-through and reagent cross-talk, as well as correction of chromatic aberration. This allows the spatial relationships of four biomolecule species to be precisely determined in a single sample. In this protocol, two fluorophores excited by a 488 nm laser line are utilized, one of which exhibits a long Stokes shift of 165 nm ((ATTO-TEC GmbH, n.d.; Coons et al., 1942); Figure 3.1). Following IF labeling, we describe general aspects of image acquisition including laser and filter selection on a confocal microscope (Basic Protocol 2).

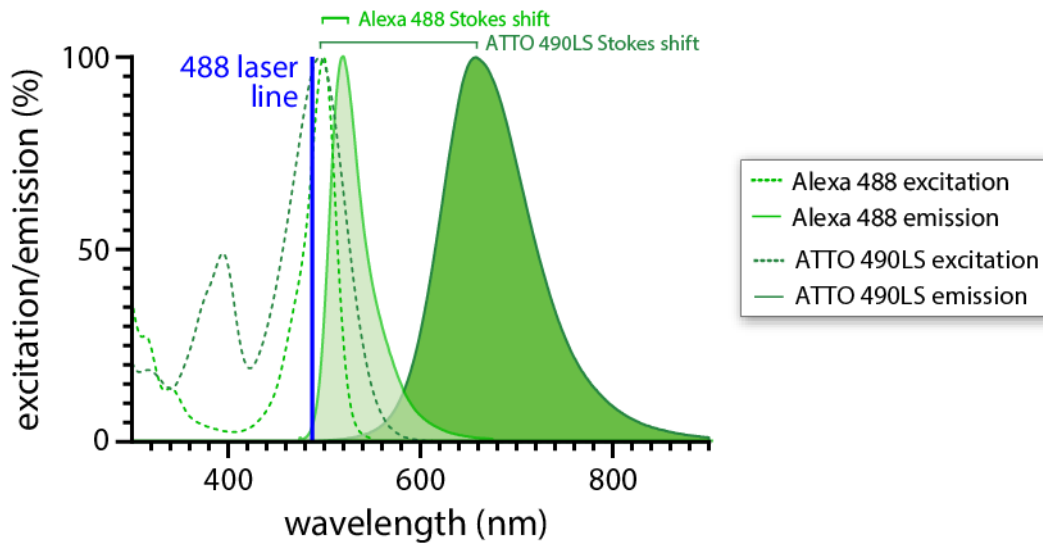


**Figure 3.1. Excitation and emission spectra of Alexa Fluor 488 (light green) and ATTO 490LS (dark green).** The 488 nm laser line is indicated (blue line). Note relative lack of overlap of emission spectra despite overlapping excitation spectra, due to long Stokes shift of ATTO 490LS(ATTO-TEC GmbH, n.d.; “Fluorescence SpectraViewer,” n.d.).

## 3.2 Strategic Planning

Appropriate controls (Table 3.1) are paramount for ensuring that both primary and secondary reagents (antibodies or streptavidin) bind solely to the expected antigen, to ensure the absence of spectral cross-talk or problematic background, and to correct for chromatic aberrations so that accurate spatial relationships can be precisely determined. The relative importance of these confounds will depend upon the specific application. The below protocol describes strategies designed to rigorously avoid—or at minimum, reveal the contribution of—such confounds. Simpler alternatives, appropriate for some applications, are also briefly introduced below.

This protocol employs no-primary, no-label, and channel alignment controls. No-primary controls, a panel of controls that each lack only one of the four primary antibodies, ensure that non-specific binding and spectral cross-talk are avoided, or at least measured. Single color controls, in which a single primary-secondary-fluorophore combination is used in isolation, are simpler to perform and sufficient for many applications. We have found, however, that commercial secondary antibodies frequently cross-bind at low levels with non-targeted primary antibodies. Though spectral cross talk can be assessed with single color controls, such cross-binding cannot be measured.

No-label controls consist of tissue not treated with any primary or secondary labeling reagents. These controls give a means to quantify autofluorescence and other sources of background. The channel alignment control, a tissue sample in which a single primary antibody is labeled with a cocktail of secondary reagents containing all four fluorophores, offers a means to quantify and correct chromatic aberrations specific to both the imaging system and the sample. A more straightforward alternative entails the imaging of fluorescent microspheres that emit in all needed wavelength ranges (e.g., ThermoFisher cat. No. T7279). This approach cannot assess aberrations

inherent to the sample itself, and the wavelengths of microsphere excitation/emission will not precisely match those of the experimental fluorophores, but they should nonetheless be adequate for many applications.

In this example, we targeted the following four antigens: glial fibrillary acidic protein (GFAP; a marker of astroglia), synapsin 1/2 (a family of presynaptic proteins), Iba1 (a marker of microglia), and CD68 (a marker of microglial lysosomes) in 50  $\mu$ m-thick, paraformaldehyde-fixed mouse brain sections. As the only unique reagent is the long Stokes shift-coupled labeling reagent, the protocol should be easily adapted to other biomolecular target combinations, fixation methods, or non-nervous tissues, though alternate or additional application-specific processing steps may be required.

Table 3.1 shows the primary and secondary antibodies that were utilized for each control sample in this example. These must be tailored to a given experiment's target antigens.

Control		Purpose	Ckn-anti-GFAP	Gp-anti-SYN	Rb-anti-Iba1	Rt-anti-CD68	Gt-anti-Ckn 647	Gt-anti-Gp Biotinylated	Streptavidin 490LS	Gt-anti-Rb 594	Gt-anti-Rt 488
No-primaries	No-GFAP	Ensure non-specific binding and spectral cross talk are measured and/or eliminated	-	+	+	+	+	+	+	+	+
	No-synapsin		+	-	+	+	+	+	+	+	+
	No-Iba1		+	+	-	+	+	+	+	+	+
	No-CD68		+	+	+	-	+	+	+	+	+
No-label	Measure autofluorescence and background	-	-	-	-	-	-	-	-	-	
Channel alignment	Measure chromatic aberration	-	+	-	-	*	+	+	+	*	*

**Table 3.1: Controls.**

\*Replace fluorophores targeting other host species with fluorophores targeting the host species of the primary antibody used in the channel alignment control. For above example, one would use Gt- $\alpha$ -Gp 647, Gt- $\alpha$ -Gp 594, and Gt- $\alpha$ -Gp 488 in lieu of the other fluorophores.

Abbreviations: GFAP, Glial Fibrillary Acidic Protein; Ckn, chicken; SYN, synapsin; Gp, guinea pig; Rb, rabbit; Rt, rat; Gt, goat.

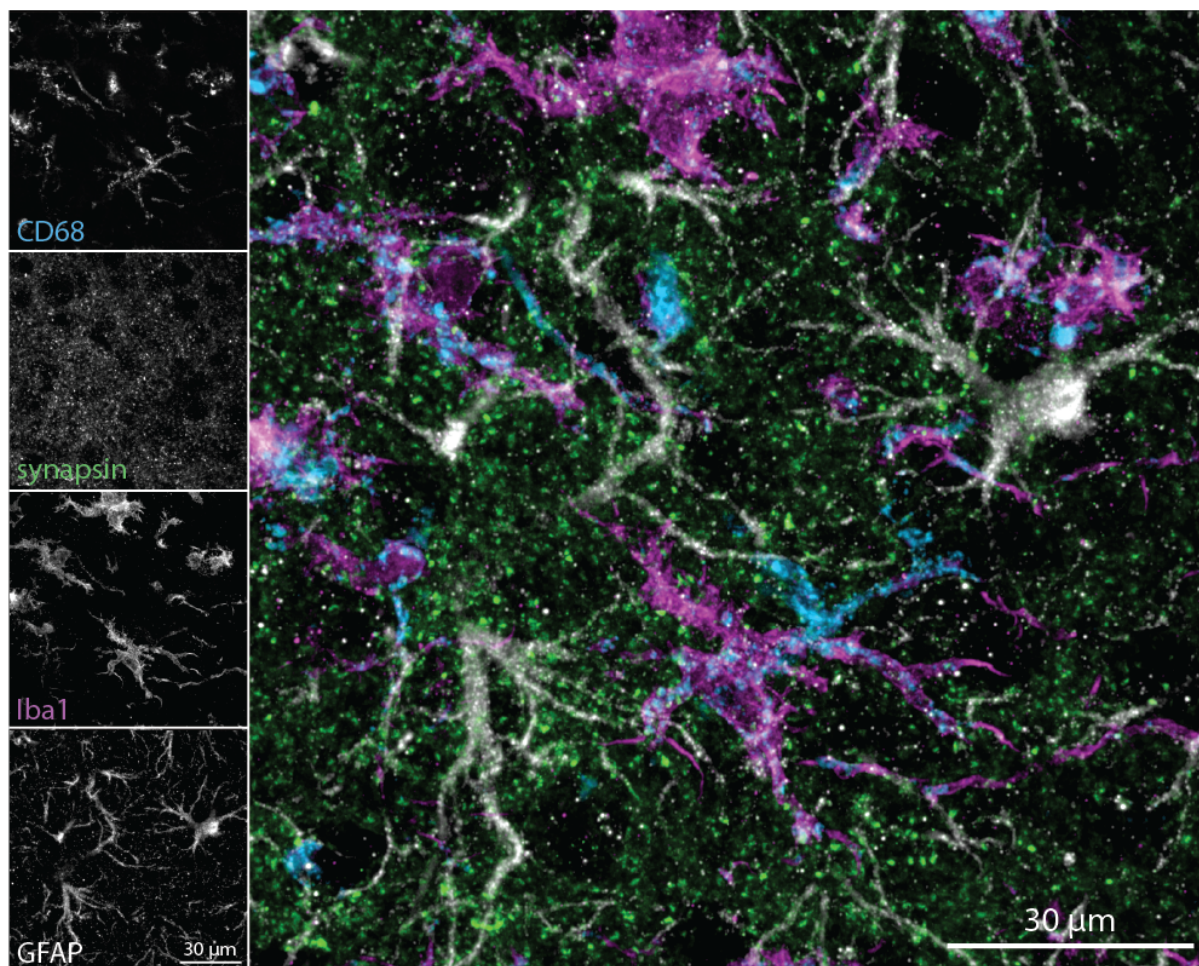


**Figure 3.2:** Image of mouse cortex co-labeled against CD68 (blue), synapsin 1/2 (green), Iba1 (magenta), and GFAP (white). Individual fluorophore label images are shown to left. Synapsin 1/2 is labeled with the long Stokes shift fluorophore.

### 3.3 Methods

#### 3.3.1 Basic Protocol 1: Four-Probe Immunofluorescence Labeling

##### Introductory paragraph:

This protocol describes immunolabeling brain tissue with primary antibodies against four target antigens followed by labeling of each primary with a spectrally separable fluorophore, including the long Stokes shift fluorophore (figure 3.1). While immunolabeling in brain tissue is described

below, this protocol could be applied to other tissue samples with appropriate antibody and section preparation modifications. The below protocol utilizes the following primary antibodies: Chicken-anti-GFAP, Guinea pig-anti-Synapsin, Rabbit-anti-Iba1, and Rat-anti-CD68. This general approach, however, should be applicable to any combination of primary antibodies that can be reliably distinguished by secondary reagents. Additionally, the below protocol describes labeling free-floating, microtome-cut 50  $\mu\text{m}$ -thick paraformaldehyde-fixed sections, but is applicable to cryostat-cut, slide-mounted tissue with minor adjustments.

Note we describe sequential labeling with two of the four antibody combinations (targeting GFAP and synapsin). This was performed to eliminate traces of cross-binding we observed between antibody species for SEQUIN analysis, a sensitive quantitative application (Reitz et al., 2021a; Sauerbeck et al., 2020). Depending on experimental goals and antibody characteristics, it may be reasonable to perform all primary followed by all secondary antibody incubations simultaneously.

***Materials:***

50  $\mu\text{m}$ -thick sections of paraformaldehyde-fixed brain tissue

Phosphate buffered saline (PBS)

6, 12, and 24 well plates

Net wells

Blocking Buffer

Antibody Buffer

Four selected primary antibodies (antibodies listed are those used below)

- Chicken-anti-GFAP (Aves Labs, cat. no. F-1005, RRID: AB\_2313547)
- Guinea pig-anti-Synapsin (Synaptic Systems, cat. no. 106004, RRID: AB\_1106784)
- Rabbit-anti-Iba1 (Wako, cat. no. 019-19741, RRID: AB\_839504)
- Rat-anti-CD68 (Invitrogen, cat. no. MA5-16674, RRID: AB\_2538168)

Three secondary antibodies conjugated with Alexa Fluor 488, 594, and 647 fluorophores (see note below under Critical Parameters, Antibody Selection)

- Goat-anti-Chicken 647 (Invitrogen, cat. no. A-21449, RRID: AB\_2535866)
- Goat-anti-rabbit 594 (Invitrogen, cat. no. A11037, RRID: AB\_2534095)
- Goat-anti-rat 488 (Invitrogen, cat. no. A-11006, RRID: AB\_2534074)

Three secondary antibodies conjugated with Alexa Fluor 488, 594, and 647 fluorophores targeting same species as biotinylated antibody (used for the channel alignment control; see Strategic Planning)

- Goat-anti-Guinea pig 488 (Invitrogen, cat. no. A11073, RRID: AB\_2534117)
- Goat-anti-Guinea pig 594 (Invitrogen, cat. no. A11076, RRID: AB\_2534120)
- Goat-anti-Guinea pig 647 (Invitrogen, cat. no. A-21450, RRID: AB\_2735091)

Biotinylated secondary antibody targeting one of the primary antibodies (in this case Goat-anti-Guinea pig; Invitrogen, cat. no. A18779, RRID: AB\_2535556)

Streptavidin conjugated ATTO 490LS (ATTO-TEC, cat. no. AD 490LS)

Tris-MWL 4-88 (Electron Microscopy Sciences, cat. no. 17977-150)

AF 300 (Electron Microscopy Sciences, cat. no. 17977-25)

Shaker

Centrifuge capable of 14,000 g

1. Move tissue sections from storage plate containing cryoprotectant to a 6 well plate containing 10-15 mL 1x PBS/well using a clean paintbrush.  
*Ensure sections are fully submerged and free to move independently. Netwells can be used in the plate to allow for easy transfer of sections between 6 well plates following the first and second rinse (step 3).*
2. Rinse sections on shaker at slow speed for 5 min at room temperature.  
*Thorough rinsing of tissue removes any remaining cryoprotectant, preparing tissue for blocking and antibody staining.*
3. Move sections to new 6 well plate with 1x PBS and rinse for 5 min.
4. Repeat steps 2 and 3 once more for a total of 3 rinses.
5. Prepare blocking buffer (see Support Protocol 1).  
*Blocking buffer can be prepared while rinsing tissue.*
6. Remove one section from wash and place in 1x PBS at 4° C.  
*This section serves as no-label control (see Strategic Planning).*

7. Add blocking buffer to a 12 well plate (750  $\mu$ L/well) and move sections using a clean paintbrush.

*Blocking buffer should be prepared with the host species of the secondary antibody (in this case goat) to minimize non-specific binding of the secondary antibody.*

8. Block for 1 hr on shaker at slow speed at room temperature.
9. Prepare antibody buffer (see Support Protocol 2).

*Antibody buffer contains Triton 100-X, a detergent that aids in antibody penetration.*

10. Add Chicken-anti-GFAP antibody to buffer at a concentration of 1:1000 and mix well.
11. Add antibody from step 10 to new plates, 750  $\mu$ L per well in a 12 well plate for up to 8 sections per well and 500  $\mu$ L per well in a 24 well plate for up to four sections per well, and move tissue using a clean paintbrush.

*The channel alignment control and no-GFAP control should not receive Chicken-anti-GFAP, but should instead be plated in antibody buffer free of antibody.*

**Optional:** *Omit the channel-alignment and no-primary control preparation in Basic Protocol [1](#). Instead, prepare a slide for channel alignment by mounting appropriate multi-fluorescent microspheres (e.g., Thermo Fisher, cat. no. T7279) on a slide in the experimental mountant. Prepare a series of single-label controls by incubating tissue sections with single primary/secondary antibody–fluorophore combinations (one for each fluorophore used for experimental labeling).*

12. Fill remaining wells with water and cover with lid.
13. Incubate 16-24 hours on shaker at room temperature.
14. Rinse 3x for 5 min each in 1x PBS (see steps 2-4).

15. Prepare antibody buffer (see Support Protocol 2).

*Antibody buffer can be stored for up to 24 hours at 4° C for use on subsequent day.*

*Antibody buffer should be at room temperature before use.*

16. Add Goat-anti-Chicken 647 secondary antibody to antibody buffer at a concentration of 1:200 and mix well.

*While modern fluorophores are generally photostable in ambient light, we protect both antibodies in solution and on tissue from light from this step forward.*

17. Add antibody solution from step 16 as necessary in 12 (750  $\mu$ L/well) or 24 well plates (500  $\mu$ L/well).

18. Transfer sections from wash to appropriate well containing secondary antibody using a clean paintbrush.

*All sections but the channel alignment control should receive Goat-anti-Chicken 647. The channel alignment control should be placed in antibody buffer free of antibody.*

19. Incubate 4 hours on shaker at room temperature.

20. Transfer tissue to 6 well plate containing 1x PBS using a clean paintbrush and rinse 3x for 5 min (see steps 2-4).

21. Prepare second primary by adding Guinea pig-anti-Synapsin at a concentration of 1:500 to antibody buffer prepared in step 15 and mixing well.

22. Plate antibody from step 21 as necessary in 12 (750  $\mu$ L/well) and 24 well plates (500  $\mu$ L/well) and transfer sections from wash to antibody with a clean paintbrush.

*No-synapsin control should be placed in antibody buffer free of antibody.*

23. Fill remaining wells with water and cover with lid.

24. Incubate 16-24 hours on shaker at room temperature.

25. Transfer tissue to 6 well plate containing 1x PBS using a clean paintbrush and rinse 3x for 5 min (see steps 2-4).
26. Prepare fresh antibody buffer (see Support Protocol 2).
27. Prepare antibody solution by adding biotinylated Goat-anti-Guinea pig to antibody buffer at a concentration of 1:200 and mix well.
28. Prepare antibody for the channel alignment control by removing 500  $\mu$ L from the antibody solution prepared with biotinylated Goat-anti-Guinea pig and adding Goat-anti-Guinea pig 594, Goat-anti-Guinea pig 647, and Goat-anti-Guinea pig 488, all at a concentration of 1:200. Mix well.  
*All fluorophores are added to the channel alignment section at the same time to allow simultaneous labeling.*
29. Add antibody solution from steps 27 and 28 as necessary in 12 (750  $\mu$ L) or 24 well plates (500  $\mu$ L) and transfer sections from wash to antibody with a clean paintbrush.  
*The channel alignment control receives a different solution, prepared in step 28, than other experimental sections and controls.*
30. Cover plates with lids and incubate on shaker at a slow speed in the dark for 4 hours at room temperature.
31. Transfer tissue to 6 well plate containing 1x PBS using a clean paintbrush and rinse 3x for 5 min (see steps 2-4).
32. Prepare labeling solution by adding Streptavidin 490 LS to antibody buffer prepared in step 26 at a concentration of 1:200 and mix well.

33. Add labeling solution from step 32 as necessary in 12 (750  $\mu$ L) or 24 well plates (500  $\mu$ L) and transfer sections from wash with a clean paintbrush.

*All experimental and control sections receive the same treatment in this step.*

34. Cover plates with lids and incubate on shaker at a slow speed in the dark for 4 hours at room temperature.

35. Transfer tissue to 6 well plate containing 1x PBS using a clean paintbrush and rinse 3x for 5 min (see steps 2-4).

36. Prepare master-mix antibody solution for Rabbit-anti-Iba1 (working concentration of 1:500) by adding antibody to antibody buffer prepared in step 26 at double the working concentration of antibody (1:250). Mix well.

*Master-mix antibody solutions are used when two or more primary antibodies are applied simultaneously to help minimize pipetting errors.*

37. Prepare master-mix antibody solution for Rat-anti-CD68 (working concentration of 1:400) by adding antibody to antibody buffer prepared in step 26 at double the working concentration of antibody (1:200). Mix well.

38. Combine master-mixes with each other (for experimental sections) and with antibody buffer (for no-primary controls) such that all solutions are diluted to appropriate working concentrations and mix well.

39. Place the channel alignment control in fresh 1x PBS, protect from light, and refrigerate at 4° C.

*The channel alignment labeling is complete and will remain in refrigerator until all sections are ready to be mounted.*

40. Add antibody prepared in step 38 as necessary in 12 (750  $\mu$ L) or 24 well plates (500  $\mu$ L) and transfer sections from wash to antibody with a clean paintbrush.
41. Fill remaining wells with water and cover with lid.
42. Incubate 16-24 hours on shaker at room temperature, protected from light.
43. Transfer tissue to 6 well plate containing 1x PBS using a clean paintbrush and rinse 3x for 5 min (see steps 2-4).
44. Prepare fresh antibody buffer (see Support Protocol 2).
45. Add Goat-anti-Rabbit 594 and Goat-anti-Rat 488 secondary antibodies to antibody buffer at a concentration of 1:200 and mix well.  
*As all tissue receives the same combination of fluorophores; master-mix creation is not necessary when combining multiple secondary antibodies.*
46. Plate antibody from step 45 as necessary in 12 (750  $\mu$ L) or 24 well plates (500  $\mu$ L).
47. Transfer sections from wash to appropriate well containing secondary antibody using a clean paintbrush.
48. Cover plates with lids and incubate on shaker at a slow speed in the dark for 4 hours at room temperature.
49. Prepare Mowiol mounting media by adding AF 300 to MWL 4-88 at a ratio of 1:9 and vortexing well. Spin in a benchtop centrifuge until bubbles are no longer present.  
*Mounting media should be prepared fresh day of use. Following preparation, store in dark at room temperature until ready to be used.*  
*Calculate amount to prepare based on 150-200  $\mu$ L/slide, preparing a minimum volume of 250  $\mu$ L.*

*MWL 4-88 is a hardening mounting media whose refractive index increases as it cures, which reduces spherical aberration, a fluorescent aberration caused by light scatter. AF 300 is an anti-fade agent which reduces fluorophore fade over time.*

*Depending on the sensitivity of the planned experiment to spherical aberrations, other mountants may be used.*

50. Prepare clean coverslips.
51. Retrieve channel alignment and no antibody control tissue.
52. Transfer both tissue finishing secondary incubation and controls from step 51 to 6 well plate containing 1x PBS using a clean paintbrush and rinse 3x for 5 min (see steps 2-4).
53. Mount free-floating tissue in 1x PBS on a charged slide and allow to dry at room temperature in a flat, dark environment (~5-10 minutes).
54. Dunk slide in distilled water 5 times very quickly to remove salt residue and allow to dry again at room temperature in a flat, dark environment (~2-10 minutes).
55. Apply 150-200  $\mu$ L mounting media/slide, dotting the mountant on tissue sections. Care should be taken to not touch sections with pipette tip.
56. Slowly apply coverslip and allow excess mountant to be expelled from under the coverslip.
57. Store slides in dark at room temperature.

*We recommend allowing Mowiol to cure for at least 3 days before imaging, as refractive index of mounting media takes several days to increase and plateau.*

### 3.3.2 Basic Protocol 2: Four-Probe Immunofluorescence Imaging

#### Introductory paragraph:

This protocol describes imaging tissue labeled with four immunofluorescent probes, including the long Stokes shift fluorophore. While the presented data was acquired using a Zeiss LSM 880 confocal microscope, any fluorescence microscope, confocal or otherwise, with appropriate light source(s) for exciting the necessary fluorophores, and with the filters necessary to adequately separate their emissions, can be used.

#### *Materials:*

Labeled, mounted tissue from Basic Protocol 1

Fluorescence microscope

Immersion oil (optional, for use with oil objective)

Lens paper

Lens cleaner

Lab wipes

1. Turn on microscope and all lasers/light sources that are needed.

*The minimum laser lines needed for the current example include 488, 561, and 633.*

*Typical examples include the argon-ion laser, the helium-neon laser, the Ti:Sapphire laser, or various epifluorescent light sources. The precise laser line may differ from those above depending on the configuration of the microscope system.*

*Allow time for light sources to reach optimum performance before imaging.*

2. Clean objective with lens cleaner and lens paper, as needed.
3. Clean slide well with lens cleaner and lab wipes, as needed.
4. Configure the light sources, light path, filter sets, and detectors to optimally image each fluorophore.

*The steps needed to accomplish this step are unique to each microscope system, but certain principles apply. See Critical Parameters: Microscope Configuration (Light sources and Light path) for additional guidance.*

5. Tune the acquisition parameters and laser power to optimize signal detection while avoiding photobleaching/toxicity.

*Specifics will depend on the given experiment, system, and goal. This is best accomplished using either a non-critical sample or region. See Critical Parameters: Microscope Configuration (Acquisition parameters) for additional guidance.*

6. Set any remaining parameters, including stack thickness and Z-step size, if necessary, and acquire the image or image stack.
7. Save data and perform any post-acquisition processing steps specific to the system.
8. Quantify and correct chromatic aberration by measuring the shift in puncta position (or similar structure for other biomolecular targets) in X, Y, and Z between fluorophores targeted to the same structure in the channel alignment control sample. Alternatively, measure the shift in position for individual, multispectral microspheres imaged along with experimental tissue. Apply an appropriate correction using image processing software such as that supplied with the microscope, ImageJ/FIJI, or similar.

### 3.3.3 Reagents and Solutions

Antibody buffer (1 mL)

- 900  $\mu$ L 1x PBS
- 100  $\mu$ L Normal Goat Serum (NGS; Vector Labs, cat. no. S-1000, RRID: AB\_2336615)
- 3  $\mu$ L Triton 100-X
- Note: After thawing, centrifuge NGS at 14,000-17,000 g for 5 minutes and when pipetting, avoid pellet
- Note: Antibody buffer can be prepared by adding 1x PBS to blocking buffer in a 1:1 ratio and then adding Triton 100-X

Blocking buffer

- 800  $\mu$ L 1x PBS
- 200  $\mu$ L Normal Goat Serum
- Note: After thawing, centrifuge NGS at 14,000-17,000 g for 5 min and when pipetting, avoid pellet

### 3.3.4 Time Considerations

When using the four primary antibodies used in Basic Protocol 1, tissue labeling requires three overnight incubations, lasting four days in sum. Performing this labeling fully in parallel would reduce this to one overnight incubation (see Basic Protocol 1 and Troubleshooting for notes on choosing parallel or sequential antibody labeling). Following labeling, we recommend the mounting media be left to cure for at least three days to reach an optimal refractive index before

imaging. Duration of image acquisition will vary between systems, imaging parameters, and the amount of imaging data required.

## 3.4 Critical Parameters

### *Antibody Selection*

Proper antibody selection is critical to ensuring minimal antibody cross-binding and nonspecific staining. When choosing primary and secondary antibodies, be sure to choose antibodies raised in species that can be adequately distinguished by secondary reagents. One can further mitigate species cross-binding by using highly cross-absorbed secondary antibodies, such as those listed in Basic Protocol 1.

### *Microscope Configuration (refer to Figure 3.3)*

Light sources: The 488 (or similar) laser line (or the Ti:Sapphire laser with appropriate tuning, or an epifluorescent light source with appropriate emission filter) will be needed to image the Alexa Fluor 488- and ATTO 490LS-labeled biomolecules. The 561 laser line (same alternates as above) will be needed to image the Alexa Fluor 594-labeled biomolecule. The 633 laser line (same alternates) will be needed to image the Alexa Fluor 633-labeled biomolecule.

Light path: Choosing filter sets and/or beam splitters that maximize signal from a given fluorophore while minimizing signal from others is an integral part of multiplexed immunofluorescence imaging. While scanning, many systems change laser lines and filter sets between frames. Especially when two fluorophores are excited by the same laser line (in the above example, Alexa Fluor 488 and ATTO 490LS), it is imperative that signal from only one fluorophore is able to reach the detector. This is achieved through the use of appropriate emission filters (band pass, long pass, short pass, variable, or a combination) that only permit the

desired wavelengths to reach the detector(s). Figure 3.3 demonstrates a successful strategy to achieve this on a confocal microscope with the fluorophores used in this example. For other implementations, it is often helpful to refer to an online fluorescence spectra viewer (e.g. <https://www.thermofisher.com/order/fluorescence-spectraviewer#!/>) to assist with choosing the most appropriate filter sets and/or beam splitter combinations for a given fluorophore. Such viewers are helpful in setting up all aspects of an IF experiment, but may not include all reagents or equipment available (e.g., ATTO 490LS is not currently, to our knowledge, included in online spectra viewers). If inappropriate light path configurations are selected, spectral cross talk is likely (see Troubleshooting for methods to determine whether this is occurring).

Acquisition parameters: Adjust the laser power, detector gain, scan speed, matrix size, pinhole size, and other system or application-specific parameters to achieve adequate signal to collect the image. If photobleaching/toxicity is noted after collecting a test image, move to a neighboring non-critical region/sample and reduce the laser power with concomitant changes to detector gain, pinhole size, or other parameters to compensate. The ideal parameters will represent a balance of speed, sensitivity, and resolution appropriate to the available signal, and must be experimentally determined for each system, sample, and experimental goal. For 3-dimensional acquisitions (Z-stacks) using a confocal microscope, it is important to remember that photobleaching/toxicity will occur at all Z-positions regardless of which optical section is currently being acquired. Thus acquisition parameters must be tested using the full planned experimental settings, not only for a single optical section.

### *Fluorophore Imaging Order*

As the 488 laser is used to excite both Alexa Fluor 488 and ATTO 490LS, but only one fluorophore is imaged at a time, photobleaching is a concern. While negligible in our experience, photobleaching can be minimized by imaging the fluorophore with the lower laser power requirement (generally the least abundant or antigenic biomolecular target) first.

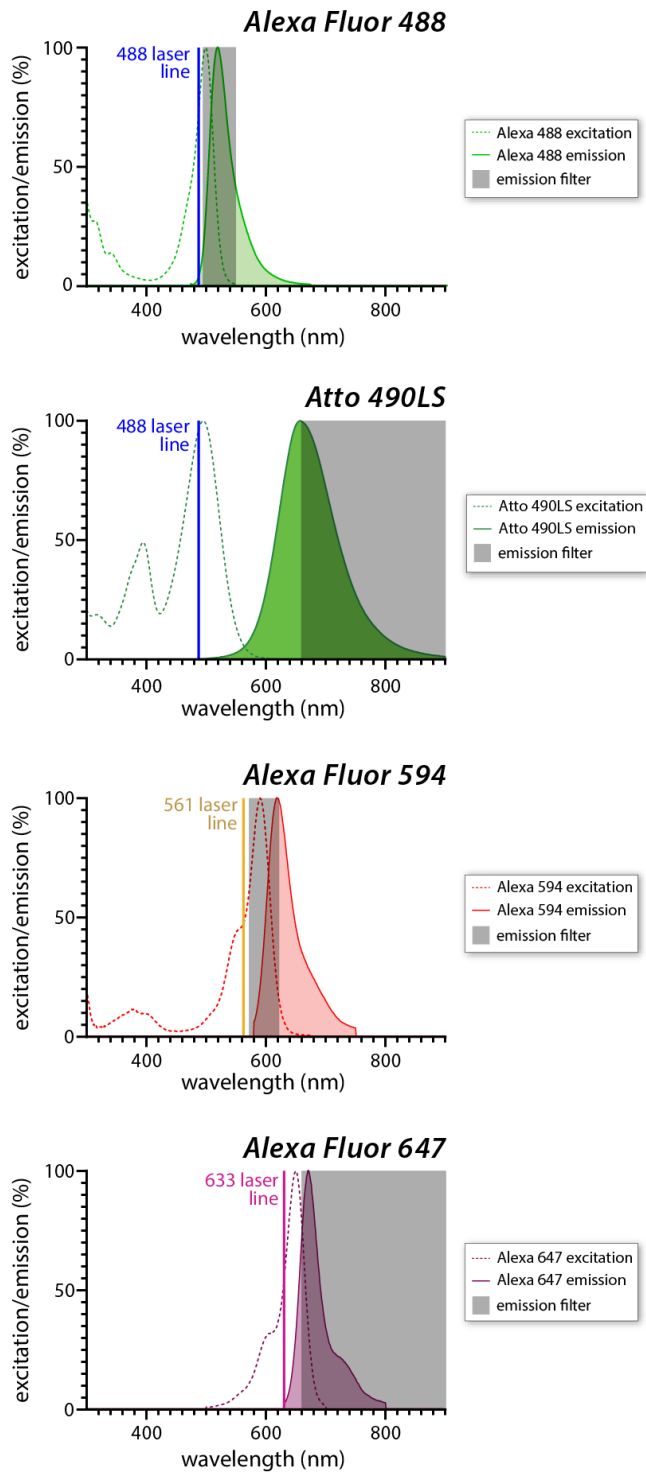


**Figure 3.3: Laser lines and choice of emission filters for imaging each fluorophore without spectral cross-talk.** The depicted filter band (grey box) corresponds to the wavelength range passed to the detector. Note that this illustrates one successful configuration; other configurations are also possible.

## 3.5 Troubleshooting

The primary issue that may arise with this approach is spectral or antibody cross-talk/cross-binding (see Understanding Results). Assuming that there was no opportunity for antibody contamination, signal from the no-primary controls (appearing to come from a primary antibody that was specifically omitted) can result from three potential sources: antibody cross-binding, spectral cross-talk, or background sources such as autofluorescence. The common signatures of these sources, as well as steps to mitigate them, are described below.

Antibody cross-binding occurs when a secondary antibody binds to an antibody other than its target and manifests as an identical (often much dimmer) image of an off-target antigen appearing in the no-primary image. That is, the fluorophore-tagged secondary antibody targeted to the omitted primary can be detected at sites where off-target antibodies are present. To mitigate antibody cross-binding, choose antibodies carefully (see Critical Parameters, “Antibody selection”). To further address problematic antibody-cross binding, antibody labeling can be separated into sequential steps. For example, in Basic Protocol [1](#), the goat anti-chicken 647 antibody demonstrated a small amount of nonspecific binding. To mitigate this, we applied the chicken anti-GFAP antibody followed by the secondary goat anti-chicken 647 antibody before other primary or secondary antibodies were applied and thoroughly rinsed the tissue to ensure that any unbound antibody was removed.

Spectral cross-talk occurs when filters inadequately separate fluorescence from two or more fluorophores. This can appear similar to antibody cross-binding. Imaging parameters, informed with online spectra viewers, should be adjusted to eliminate this cross-talk. If this fails, alternate fluorophore combinations may be required. See Critical Parameters, “Microscope configuration,” for details. If it remains unclear whether spectral cross-talk or antibody cross-binding is

responsible for artifactual signal, single-color controls (see Strategic Planning) can help resolve the issue, as antibody cross-binding is eliminated as a potential source.

Autofluorescence is light emission by endogenous tissue components (e.g., collagen, lipofuscin) or processing-related chemicals (e.g., fixative). General background can also arise from numerous other sources, including endogenous antibody sources or receptors. To evaluate the contribution of autofluorescence or other background signals, compare images from the no-label control to the problematic image. Autofluorescence can be mitigated by avoiding problematic structures, adjusting tissue processing steps, applying certain pretreatments, or, in some cases, performing computational processing post-acquisition.

### **3.6 Understanding Results**

No-primary controls, a series of controls that receive all primary antibodies except one (varies, see Table 3.1) and all secondary antibodies, elucidate the contribution of spectral cross-talk and non-specific antibody binding. While some degree of autofluorescence is common in fixed brain tissue, images from no-primary controls should exhibit very low levels of signal for the missing primary. Other targeted antigens should not be contaminated by signal from the omitted primary (Figure 3.4).

To properly assess no-primary images, it is essential that the tissue from each group (experimental samples and each no-primary control) is from the same experimental condition and labeling run, and imaged the same day using identical settings. Following image acquisition, all signals from each sample image should be intensity adjusted using identical parameters to those employed for experimental images.

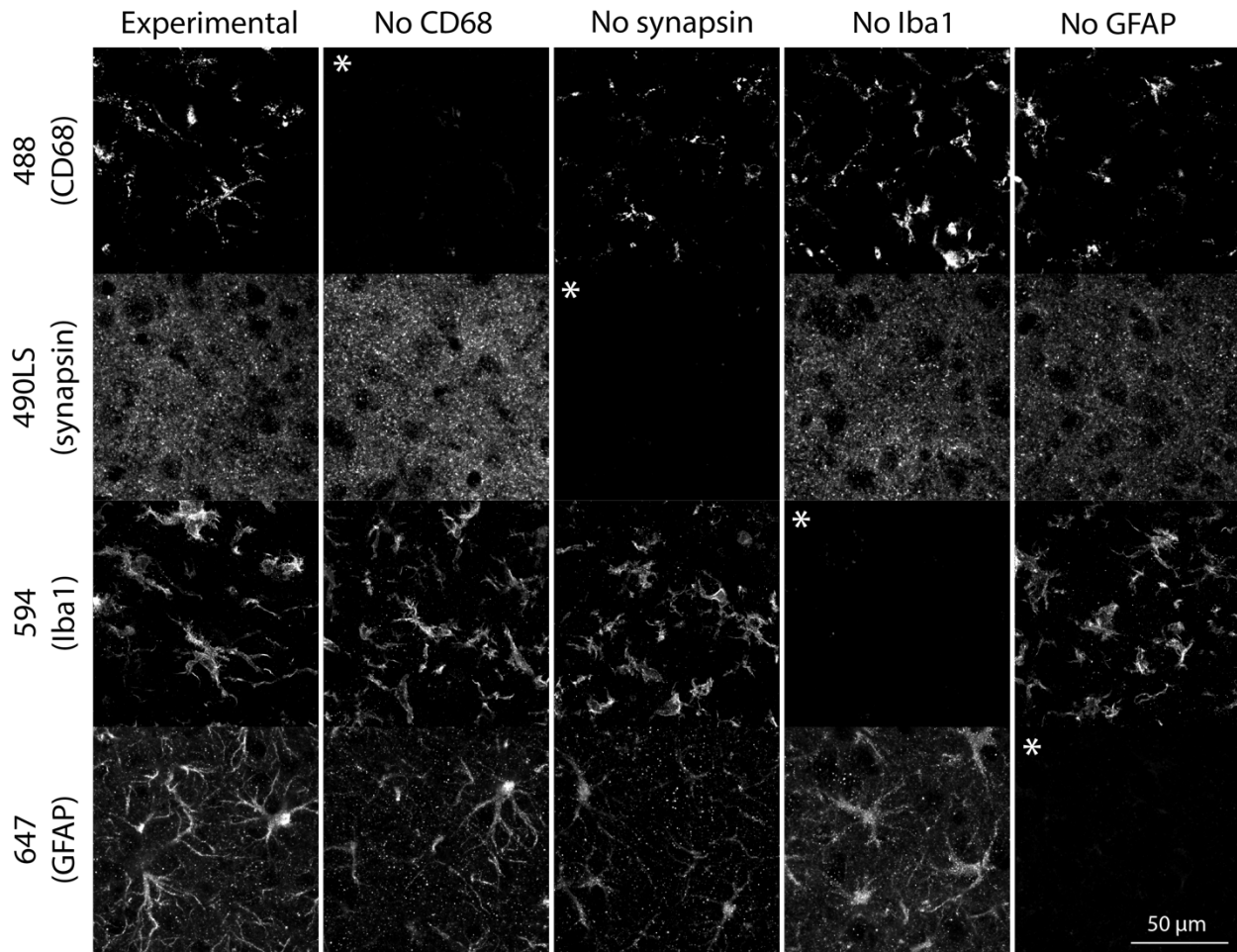


**Figure 3.4: No-primary controls revealing no spectral cross-talk or non-specific labeling.** Columns represent individual experimental or no-primary control samples (the same field is represented down the column). Fields labeled with \* represent antigens for which a primary antibody was omitted during labeling. Note lack of signal in these images.

### 3.7 Conclusions

While most lasers produce excitation light at one or a small number of discrete wavelengths, fluorophores are excited by and emit photons over a relatively broad range (*e.g.*, Figure 3.1). This leads to challenges in multiplexing probes due to the spectral overlap of emitted light. Well-equipped imaging systems can, in theory, distinguish a large number of multiplexed fluorophores in a single sample, allowing spatial relationships between fluorophores (and by extension their antigenic targets of interest) to be determined. In practice, however, a combination of system

inefficiencies, fluorophore properties, autofluorescence/background signal, and optimizations common in commercial systems frequently limit the number of multiplexed probes analyzable in a single sample to three (in approximately the blue-green, red, and infrared regions of the electromagnetic spectrum).

Exceptionally abundant target biomolecules or bright probes can, in some cases, overcome these limitations allowing greater multiplexing. For example, 4',6-diamidino-2-phenylindole (DAPI) interacting with DNA, an extremely abundant biomolecule in tissues, results in exceptionally bright ultraviolet (UV) fluorescence that can overcome the high level of UV autofluorescence in nervous tissues (Bottiroli et al., 1998; Pascu et al., 2009). Specialized probes (e.g., quantum dots, see above), optics, lasers, and detectors can in other instances enhance multiplexing capabilities, but these may not be available, or may require compromises in efficiency, probe choice, and interpretability that similarly restrict their application.

The use of a long Stokes shift fluorophore offers a relatively low-friction, accessible alternative, allowing biomolecules of average to low abundance to be specifically targeted, imaged and analyzed. This approach has several important advantages, the most important of which is its accessibility: The method relies on standard immunolabeling and is thus highly adaptable to experimental needs. Moreover it requires no additional hardware/optics or analysis approaches beyond those used in standard three-label IF applications, thus most microscopes equipped to analyze fluorescence in standard wavelengths will be equipped to image the long Stokes shifted fluorophore described above (ATTO 490LS). Limitations include the need to identify a series of primary and secondary antibodies that do not exhibit cross-binding (utilization of biotin-avidin binding is advantageous in this regard, and the above protocol includes steps to identify cross-binding). Where problematic, such cross-binding can often be overcome by sequential labeling

or direct primary antibody-fluorophore conjugation. Several kit-based labeling systems for conventional or long Stokes shift fluorophores are available to accomplish this.

The above approach provides a low-friction method to enhance the information that can be gleaned from precious biospecimens. This should assist in particular with the structural characterization of complex microscopic apparatuses such as synapses that are defined by the functional apposition of numerous and diverse molecular components(O'Rourke et al., 2012; Sauerbeck et al., 2020).

# **Chapter 4: TBI in the Aged Brain**

## **4.1 Introduction to TBI in the Aged Brain**

As previously discussed, TBI has both higher prevalence and worse outcome in an aged population as compared to adult peers (Annegers et al., 1998; Annegers and Coan, 2000; Centers for Disease Control, 2021; Green et al., 2008; Mosenthal et al., 2004). However, very little is known about mechanisms underlying this disparity. This study aimed to describe differences in microstructure, neuroinflammation, and function in 3- and 18- month old healthy mice and mice receiving and experimental TBI. To do so, a multimodal model of injury yielding both focal and diffuse pathology was employed. As the majority of moderate-to-severe human TBI is both focal and diffuse in nature, combining these modes of injury increases the model's relevance to human disease. 21 days following injury, mice underwent a behavioral battery consisting of assays of learning and memory and anxiety-like behavior, and tissue was collected at a subacute timepoint (35 days post injury). Using previously described techniques, synaptic density, nuclear band thickness, and microgliosis were all measured in the CA1 region of the hippocampus, due to this area's strong correlation with functional endpoints of interest.

## **4.2 Methods**

### **4.2.1 Animals**

All animal procedures were approved by the Washington University Institutional Animal Care and Use Committee and performed in accordance with all relevant guidelines and regulations. All experiments were performed in male C57BL/6 mice (Jackson Labs #000664, Bar Harbor, ME, USA). Mice were allowed to acclimate for 1–2 weeks prior to all studies with 12-hour light-dark cycles. Food and water was provided ad libitum. Adult animals were 3 months of age, and aged animals were 18 months old at time of injury.

#### **4.2.2 Traumatic Brain Injury**

An experimental, multimodal TBI yielding both focal and diffuse injury was generated by combining the modCHIMERA and controlled cortical impact injury models. ModCHIMERA was completed first at an impact energy of 2.1 J, as previously described(Sauerbeck et al., 2018), followed by unilateral controlled cortical impact at a depth of 1.5 mm, as previously described(Brody et al., 2007). Briefly, anesthesia was induced with 5% isoflurane (Covetrus, Portland, ME, USA, cat# 029405). Anesthesia was maintained at 2.5% isoflurane for the duration of modCHIMERA positioning. A semi-rigid helmet fashioned from Tygon S3 B-44-4 × tubing (5/16-inch inner diameter/1/2-inch outer diameter) was secured on the animal's head and the animal was positioned supine on the CHIMERA stage(Sauerbeck et al., 2018) and secured in the holder(Sauerbeck et al., 2018). 30 seconds prior to impact the anesthesia was discontinued and the pneumatically-driven piston was fired at the set energy. Following impact, animals were placed back on anesthesia at a reduced level of 1.5% isoflurane and mounted in a stereotaxic frame without waking. Animals then received subcutaneous Buprenorphine ER (1 mg/kg)(ZooPharm, Fort Collins, CO, USA), the scalp was shaved, betadine was applied to the scalp, and petroleum lubricant applied to the eyes. The top of the skull was exposed with a 1 cm incision, and a 5 mm craniotomy was performed with a trephine (Fine Science Tools Inc., Foster City, CA, USA, cat# 18004-50) over the left parietotemporal cortex. A 3 mm metal impactor tip was centered 3.0 mm anterior to lambda and 2.7 mm left of midline at an angle of 15°. An impact injury was induced using an electromagnetic impactor delivered a 1.5 mm depth impact with 100 ms dwell time, at a velocity of 5 m/sec (Leica Biosystems, Wetzlar, DE). A 7 mm plastic cap (produced by the Washington University Machine Shop from commercially available weigh boats) was attached to the skull using Vetbond (3M, St. Paul, MN, USA, cat# 1469SB) to cover the lesion. The scalp was sutured with 5-0 nylon sutures (McKesson, Irving, TX, USA,

cat# S661GX), and animals were allowed to recover in an incubator maintained at 30° C. Sham animals were anesthetized under the same conditions and underwent positioning on the CHIMERA device, but the piston was not fired. They were then mounted in the stereotaxic frame under anesthesia where they received Buprenorphine ER (1 mg/kg), an identical scalp incision, and skull drilling (marking of at least 70% of the diameter of the trephine without penetration of the skull inner table). The incision was closed with sutures. Sham animals also received Buprenorphine ER. The model yielded a mortality rate of 22.2% in 3 month old mice and 32% in 18 month old mice. Animals that lost >20% total body weight following TBI were excluded from the study (12% of 18 month old mice, no 3 month old mice).

#### **4.2.3 Behavior**

Behavior was conducted in a dedicated behavior room during daytime hours. The room was equipped with light, sound, and humidity controls and insulated from external noise. Mice were allowed to acclimate in this room for at least 24 hours prior to testing. Illuminance was measured and set independently at the start of each test (40 lux for Morris water maze testing; 20 lux for all other tests) using a lux meter (Sper Scientific 840006, Scottsdale, AZ, USA) at the level of the test apparatus. A white noise machine (Marpac Dohm-DS, Wilmington, NC, USA) was set to deliver 60 dB at the test apparatus as measured with a decibel meter (Lafayette Instrument SL-A, Lafayette, IN, USA). To eliminate scents, all testing surfaces were thoroughly cleaned with 70% ethanol prior to testing and between animals. For Open Field Test, Y-maze, and Morris Water Maze testing an overhead camera recorded all mouse paths, which were subsequently processed using SMART (Panlab/Harvard Apparatus, Barcelona, Spain) and Pathfinder (<https://github.com/MatthewBCooke/Pathfinder>).

For use of the open field test, mice were individually placed in the corner of a custom 44.5 × 44.5 cm opaque box 21 days post-injury and allowed to explore for 5 minutes. To monitor thigmotaxic behavior, average distance from the wall of the open field box was calculated by defining square, concentric zones spaced 1.5 cm apart (15 in total) using SMART and deriving a time-weighted average (Sauerbeck et al., 2018).

The Y-maze test was performed using a custom-built apparatus composed of three arms each separated by 120°. Each arm was 30 cm long and 6 cm wide. Walls were opaque white, 15 cm tall. Mice were placed in the distal end of one arm and allowed to explore for 8 minutes. Number and order of arm entries were calculated using SMART. Success was measured as percent alternations, or the number of times the animal moved in a non-repeating pattern from arm to arm (e.g., A→B→C), divided by all triwise movements.

For the Morris Water Maze, a 120 cm diameter pool (source), made opaque by the addition of white tempera paint, was used for all trials and a platform was placed 1 cm below the surface. Prominent visual cues were hung at intervals around the maze. Mice underwent four trials each day across six days of hidden platform training starting 23 days post-injury. They were inserted into the pool at a different location for each trial and the order of the insertion points was changed daily. The day following hidden platform testing mice underwent a single probe trial in which the platform was removed and mice were inserted at a consistent, distant point from the prior platform location. Mice then completed 5 days of visible platform testing, with the escape platform relocated to a new quadrant of the pool and raised above the water, and a flag placed in the center of the platform. Threshold for visual function was set as an average swim distance to the platform on one or more days of visible testing better than (below) the 5<sup>th</sup> percentile of sham performance on the first day of hidden platform testing.

#### **4.2.4 Tissue Collection**

At 35 days post-injury mice were euthanized and transcardially perfused with ice cold phosphate buffered saline (PBS, Corning Inc., Corning, NY, USA, cat# MT-46013CM) followed by ice cold 4% paraformaldehyde in PBS (PFA, ThermoFisher Scientific, Waltham, MA, USA, cat# AC416785000) for 5 minutes. Brains were then extracted and post-fixed in PFA overnight at 4°C followed by equilibration in 30% sucrose in PBS for at least 24 hrs. Brains were sectioned on a freezing microtome (Microm HM 430, ThermoFisher Scientific, Waltham, MA, USA) at 50 µm. Sections were stored in a cryoprotectant solution (30% sucrose and 30% ethylene glycol in PBS; Fisher Scientific, Waltham, MA, USA, cat# S5-500; Fisher Scientific, Waltham, MA, USA, cat# E178-4) at -20 °C.

#### **4.2.5 Immunohistochemistry**

The following primary antibodies were used: PSD-95 (Invitrogen, Waltham, MA, USA, cat. #51-6900, 1:200), synapsin (Synaptic Systems, Goettigen, Germany, cat. #23400`9, 1:1000), Iba1 (Synaptic Systems, Goettigen, Germany, cat. #106004, 1:500), CD68 (Invitrogen, Waltham, MA, USA, cat. #MA5-16674, 1:400), and Ki67 (abcam, Waltham, MA, USA, cat. #ab16667, 1:500). The following secondary antibodies were used: Alexa Fluor goat-anti rabbit 594 (Invitrogen, Waltham, MA, USA, cat. #A-11037, 1:200), Alexa Fluor goat-anti guinea pig 488 (Jackson ImmunoResearch, West Grove, PA, USA, cat. 106-545-003, 1:200), Alexa Fluor goat-anti chicken 647 (Invitrogen, Waltham, MA, USA, cat. # A-21449, 1:200), Alexa Fluor goat-anti rat 647 (Invitrogen, Waltham, MA, USA, cat. #A-21247, 1:200), and Alexa Fluor biotinylated goat-anti chicken (Invitrogen, Waltham, MA, USA, cat. #PA1-28797, 1:200). Sections were rinsed with PBS (Corning Inc., Corning, NY, USA, cat# MT-46013CM), blocked with 20% normal goat serum (Vector Labs, Burlingame, CA, USA, cat. #S-1000) in PBS, and incubated with primary antibodies in 10% normal goat serum with 0.3% Triton X-100 (Sigma-Aldrich, St.

Louis, MO, USA, cat. #T8787) overnight at room temperature. The following day, sections were rinsed with PBS, and incubated in secondary antibodies in 10% normal goat serum with 0.3% Triton X-100 for 4 hrs at room temperature. Sections treated with biotinylated goat-anti chicken antibody were subsequently incubated for 4 hours at room temperature with streptavidin-conjugated ATTO 490LS (ATTO Technology, Amherst, NY, USA). Tissue was rinsed with PBS, labeled with DAPI, and rinsed with PBS a final time before being mounted on slides in PBS. Sections were allowed to fully dry in the dark, then were rinsed with brief dips in distilled water, allowed to dry again, and coverslipped using Mowiol 488 mounting media with Antifade 300 (Electron Microscopy Services, Hatfield, PA, USA, cat# 17977-150, cat# 17977-25) mixed at a 1:9 ratio and H1.5 coverslips (Paul Marienfeld GmbH & Co., Lauda-Königshofen, DE, cat# 0107242).

#### **4.2.6 Image Collection**

All images except those used for nuclear band thickness were acquired using a Zeiss LSM 880 microscopy with AiryScan detector (Zeiss Group, Oberkochen, Germany). All analyses were conducted in the hemisphere ipsilateral to the side of focal injury. For synapse quantification and lysosome/endosome analysis, images were acquired from the CA1 molecular layer using a 63x 1.4 NA oil immersion objective with a magnification of 1.8x as a 2x2 tile scan with 10% overlap between tiles. The total axial size of the imaged regions was 141.40  $\mu\text{m}$  x 141.40  $\mu\text{m}$ . Step size was 120 nm and 35 slices were acquired, for a total image thickness of 4.08  $\mu\text{m}$ . The Z stack was centered equidistant from the section upper and lower cut surfaces. For microglial density and proliferation, images were acquired from the CA1 molecular layer using a 20x 0.8 NA air immersion objective, with a magnification of 2x. The axial image size was 212.55  $\mu\text{m}$  x 212.55  $\mu\text{m}$ . Step size was 500 nm and 21 slices were acquired, for a total image thickness of 10.5  $\mu\text{m}$ .

The Z stack was centered equidistant from the section upper and lower cut surfaces. For nuclear band quantification, images were acquired using the Zeiss Axioscan 7 Slide Scanner with a 20x 0.8 NA air immersion objective (Zeiss Group, Oberkochen, Germany).

#### **4.2.7 Image Processing and Analysis**

All post-acquisition image processing utilized Zen black software (Zeiss Group, Oberkochen, Germany). For synapse quantification and lysosome and endosome analysis, all images were AiryScan processed using a strength of 6. Chromatic aberration was quantified using experimental tissue for which one punctate epitope (synapsin) was labeled with all three utilized fluorophores (Alexa 488, 594, and 647; Invitrogen, Waltham, MA, USA). Separation between identical puncta images in different acquisition channels was calculated, and images were shifted to correct chromatic aberration. All images acquired for microglial density and proliferation analysis were AiryScan processed using the system's automatically-determined strength. No chromatic aberration correction was required for these images.

Synapse quantification was performed using the SEQUIN technique as previously described with the following modifications (Reitz et al., 2021a; Sauerbeck et al., 2020). Briefly, following AiryScan processing and chromatic aberration correction, spots detection was performed using Imaris (Bitplane, Belfast, UK) for the presynaptic protein synapsin and the post-synaptic protein PSD-95 at a puncta size of 0.2  $\mu\text{m}$  x 0.6  $\mu\text{m}$ . The distance between the centroid of each PSD-95 punctum was then measured from its nearest neighboring synapsin punctum using SEQUIN code (<https://github.com/KummerLab/SEQUIN>) running in Matlab (Mathworks, Natick, MA, USA). The 20% brightest puncta from each subset were included in the analysis (Sauerbeck et al., 2020). Synaptic density was determined by summing all colocalized PSD puncta with a nearest neighboring synapsin punctum nearer than 280 nm (Sauerbeck et al., 2020).

Nuclear band thickness was measured at three points along the CA1 nuclear band using ImageJ. The first point was located at the superior-most point of the nuclear band, and the second two measurements were taken 500  $\mu\text{m}$  medially and laterally of the first point. Thickness was averaged across all three points. Animals with lesions interrupting the nuclear band preventing measurement at all three points were excluded from this analysis.

Microglia were manually counted by one blinded investigator using ImageJ (U.S. National Institutes of Health, Bethesda, MA, USA). To do this, the images were adjusted for brightness and contrast to optimize visibility of microglial cells. Cells partially out of frame on the top and right edges of the image were counted only if more than 50% of the cell body was visible within the field of view, and cells partially out of frame on the bottom and left edges of the frame of view were not counted. Care was taken to ensure that overlapping cells were not counted twice. In cases where cell boundaries were not clearly distinguishable, cells were excluded from the count to avoid overestimation. To quantify EdU<sup>+</sup> microglia and Ki67<sup>+</sup> microglia, the same method was applied, but only selecting cells positive for both Iba1 and either EdU or Ki67.

Using Imaris, endosome and lysosome volume per field was calculated by creating CD68<sup>+</sup> surfaces using a voxel intensity threshold ( $\geq 4,000$  u) and number of connected voxels threshold ( $\geq 100$ ). To isolate synapsin and PSD-95 signal within these lyso-endosomal structures, signal originating from these markers limited to within the CD68<sup>+</sup> surfaces.

#### **4.2.8 Cellular Proliferation Assay**

To assess acute cellular proliferation, at 3 days post-injury animals received an intraperitoneal injection of thymidine analog 5-Ethynyl-2'-deoxyuridine (EdU) (50 mg/kg) (Invitrogen, Waltham, MA, USA, cat. #A10044). To detect EdU, tissue sections were rinsed in PBS, blocked for 1 hr in 20% normal goat serum with 0.3% triton X-100, rinsed again with PBS, and incubated

in the reaction cocktail for 30 min as described by the manufacturer (Invitrogen, Waltham, MA, USA, cat. #C10640). To co-label with antibodies, tissue was again rinsed in PBS, and antibody labeling conducted as described above.

### **4.2.9 Statistics**

All results were tested for normality using the Shapiro-Wilk test. For all tests,  $p < 0.05$  was considered significant. Non-normally distributed data was transformed where able. With the exception of data related to hippocampal integrity (figure 4.2), a two-way ANOVA was applied to all normally-distributed data, followed by the Tukey post-hoc test. For hippocampal integrity, a Fisher's exact test was applied. The Mann-Whitney U test followed by the Holm-Bonferroni method to correct for multiple comparisons was used in non-normally distributed data that could not be transformed. All tests were 2-sided. GraphPad Prism was used for all statistics (GraphPad Software, San Diego, CA, USA).

## **4.3 Results**

### **4.3.1 Excitatory Synaptic Density**

Excitatory synaptic density was quantified using SEQUIN, a super-resolution imaging and analysis technique that identifies synaptic loci by virtue of the characteristic separation distance between pre- and postsynaptic markers. The molecular region of CA1 ipsilateral to the side of focal injury was selected for investigation of synaptic density due both to the region's proximity to the lesion and the region's well-established role in learning and memory (Dong et al., 2021; Tsien et al., 1996) (figure 4.1B). All assessments were carried out 35 days post-injury (figure 4.1A). Multimodal TBI significantly reduced synapse number in both adult and aged animals compared to sham controls (adult sham mean=0.054, adult TBI mean=0.041, Cohen's  $D=1.05$ ; aged sham mean 0.057, aged TBI mean=0.041, Cohen's  $D=1.28$ ) in CA1 (figure 4.1



### 4.3.2 CA1 Neuron Loss

To probe the effect of multimodal TBI on neuron loss in the hippocampus, CA1 pyramidal neurons were quantified by measuring CA1 nuclear band thickness. Aged, sham-injured animals had a small but statistically significant reduction in CA1 nuclear band thickness compared to adult, sham-injured animals (adult sham mean=42.88, aged sham mean=41.32, Cohen's  $D=.30$ ) (figure 4.2A, D). In a subset of animals who underwent experimental TBI, multimodal TBI resulted in loss of hippocampal tissue precluding measurement of the CA1 nuclear band. CA1 nuclear band thickness was unmeasurable in 39% of adult TBI animals (7 of 18) and substantially more aged TBI animals (75%; 9 of 12), though this difference did not reach statistical significance ( $p = 0.072$ ). In the subset of TBI animals in which the CA1 nuclear band could be assessed fully, there was no clear difference in nuclear band thickness compared to age-matched shams (adult TBI mean=44.02, Cohen's  $D=0.19$ ; aged TBI mean=42.43, Cohen's  $D=0.29$ ). Thus age at time of injury appears to enhance lesion size from multimodal TBI without enhancing loss of CA1 neurons in animals without macroscale hippocampal lesions.

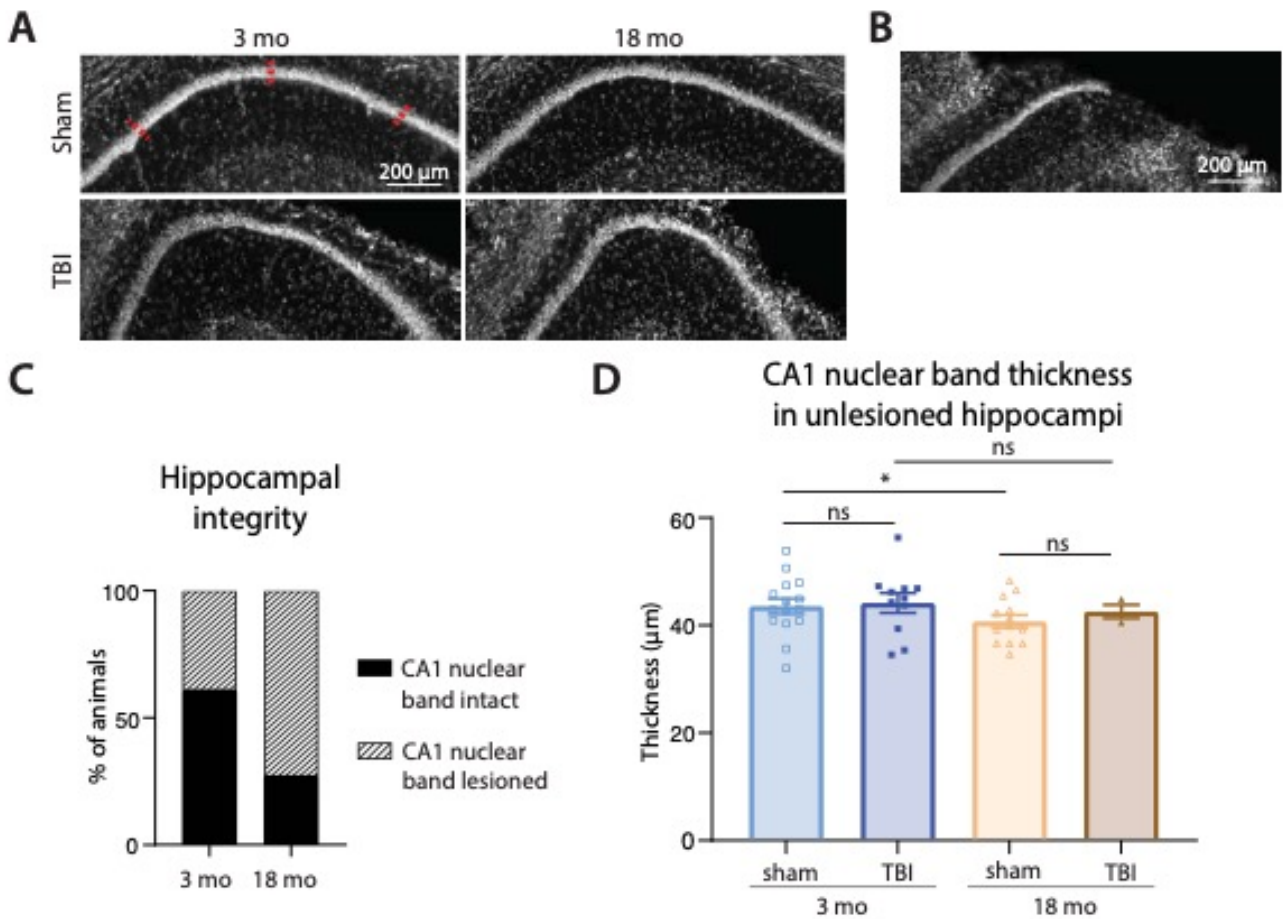


**Figure 4.2 TBI and age effects on CA1 nuclear band thickness.**

A. Representative images of intact CA1 nuclear bands from each group, DAPI used for visualization of nuclei. Dashed red line indicates locations of thickness measurement. B. Example of hippocampus with lesion precluding measurement of CA1 nuclear band thickness. C. Ratio of animals with intact vs. lesioned hippocampi as a function of age. D. Quantification of nuclear band thicknesses. \* $p < 0.05$

### 4.3.3 Microglial Density and Proliferation

An increase in microglial density is linked to both neurodegenerative disease and acute neuroinjury (Ganz et al., 2022; Loane et al., 2014). To evaluate the effect of TBI on microglia in adult and aged animals, their numbers were assessed. While there was no difference in microglial density between adult and aged sham-injured animals as detected by labeling with Iba1 (adult sham mean=44753, aged sham mean=47623, Cohen's  $D=0.40$ ), injury significantly increased

microglial density in both adult and aged animals compared to controls at 35 days post-injury (adult TBI mean=78326, Cohen's D=2.28;aged TBI mean=121566, Cohen's D=1.77)(figure 4.3 A,B). Aged animals subjected to TBI, moreover, exhibited greater microglial density than adult, injured animals (Cohen's D=1.05). Thus aging amplifies microglial responses to injury.

Cellular proliferation was then probed at both an acute time point (3 days post-injury) and a semi-chronic time point (35 days post-injury). To label cells undergoing mitosis at the acute time point, animals were injected with thymidine analog EdU 3 days post-injury. Density of microglia co-labeled with EdU and Iba1 increased in both adult and aged animals following TBI (adult sham mean=673.5, adult TBI mean=8959, Cohen's D=1.54;aged sham mean 0, aged TBI mean=19568, Cohen's D=1.76), but a significant of age could not be detected in either the sham-injured or the TBI condition (sham Cohen's D=0.53, TBI Cohen's D=1.01)(figure 4.3 A,C).

To measure proliferating microglia at the subacute time point of 35 days post-TBI, Ki67<sup>+</sup> microglia were quantified. No difference was observed comparing sham-injured animals at either age (adult sham mean=29341, aged sham mean=32321, Cohen's D=0.55). TBI increased Ki67<sup>+</sup> microglia in both groups (adult TBI mean=46419, Cohen's D=1.40;aged TBI mean=58860, Cohen's D=1.21), but no difference was observed between adult and aged TBI animal Ki67<sup>+</sup> microglial density (Cohen's D=0.53)(figure 4.3 D,E).

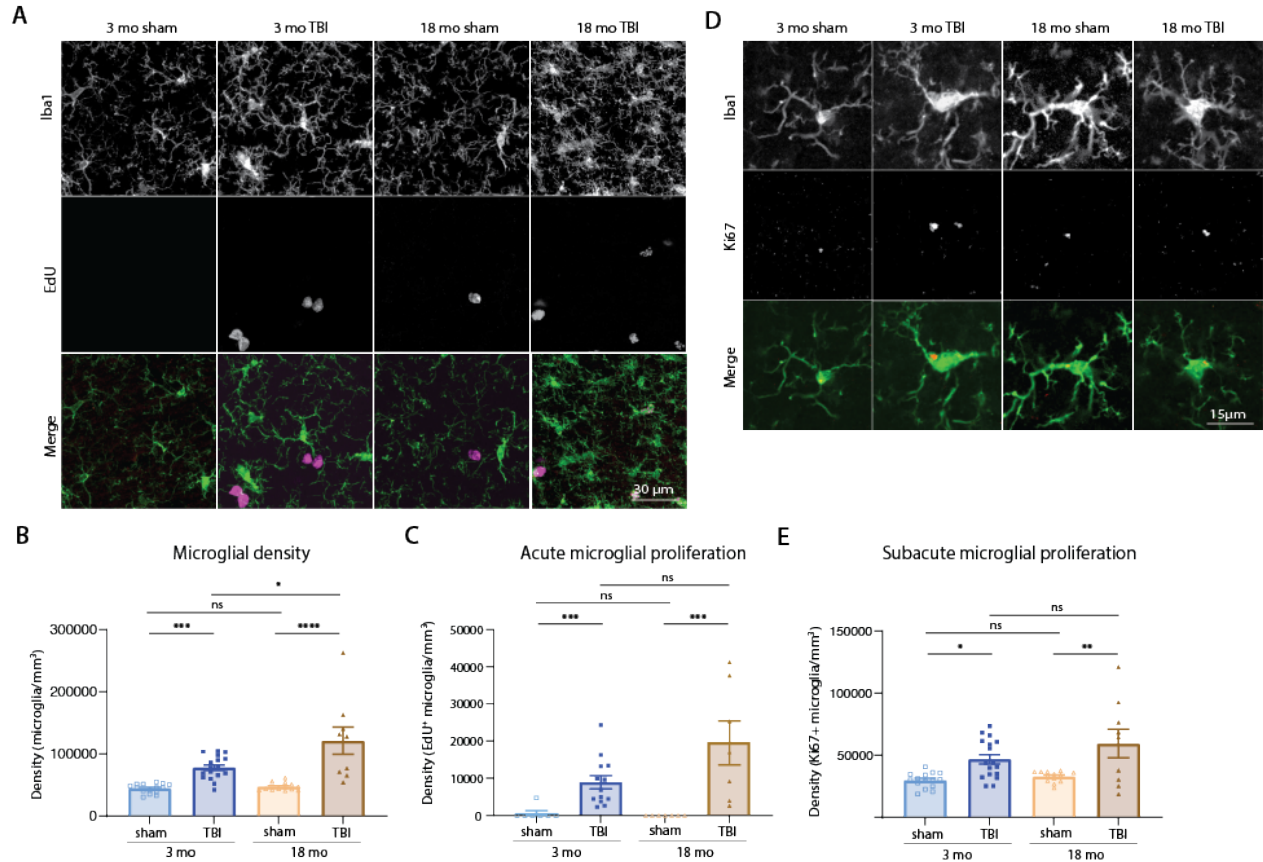


**Figure 4.3. TBI increases microglial number and enhances proliferation.**

A. Images showing microglia (Iba1), cells positive for EdU at 3 days post-injury, and the two channels merged. Images acquired from hippocampal CA1 molecular layer. B. Quantification of microglial density. C. Quantification of cells colabeled for EdU and Iba1. D. Images showing microglia (Iba1), cells positive for Ki67 at 35 days post-injury, and the two channels merged. Images acquired from hippocampal CA1 molecular layer. Quantification of cells colabeled for Ki67 and Iba1. \* $p < 0.05$ , \*\* $p < 0.01$ , \*\*\* $p < 0.001$ , \*\*\*\* $p < 0.0001$

#### 4.3.4 Synaptic Phagocytosis by Microglia

To characterize potential mechanisms of synapse loss following injury, microglial phagocytic activity was probed by measuring the volume of endosomal/lysosomal objects within microglia, as well as measuring the synaptic content of these structures.

To study the effect of TBI on the number and size of endosomal/lysosomal objects, tissue was labeled against CD68. While age does not appear to substantially modulate CD68+ volume in either the sham or injured condition (adult sham median=0.000062, aged sham median=0.000042, Cohen's D=0.60; adult TBI median=0.00025, aged TBI median=0.00065, Cohen's D=0.61), injury significantly increases CD68+ volume (adult Cohen's D=0.89; aged Cohen's D=1.40) (figure 4.4 A-C). Similarly, while age was not found to substantially modulate the number of detected CD68+ particles in either the sham or injured condition (adult sham median=169911, aged sham median=611743, Cohen's D=0.61; adult TBI median=123809, aged TBI median=929607, Cohen's D=0.54), injury significantly increased the density of CD68+ objects in both age groups (adult Cohen's D=1.54, aged Cohen's D=1.37).

To investigate synaptic phagocytic activity, PSD95 and synapsin labeling within CD68+ particles was quantified. Labeling of both PSD95 and synapsin within endosomal/lysosomal particles increased in both adult and aged animals following injury (adult sham PSD95 median=27710000, adult TBI PSD95 median=121500000, PSD95 Cohen's D=0.81; aged sham PSD95 median=17220000, aged TBI PSD95 median=355000000, PSD95 Cohen's D=25.88; adult sham synapsin median=30485575, adult TBI synapsin median=123000000, synapsin Cohen's D=0.86; aged sham synapsin median=22820000, aged TBI synapsin median=507000000, synapsin Cohen's D=1.57). However, no effect of age was observed in either condition (PSD95 sham Cohen's D=0.31, PSD95 injured Cohen's D=0.53; synapsin sham Cohen's D=0.40, synapsin injured Cohen's D=0.42) (figure 4.4 D-F). These results demonstrate that TBI increases phagocytic potential as well as synaptic phagocytosis of both pre- and postsynaptic proteins, but they do not support a differential effect of age at time of injury.

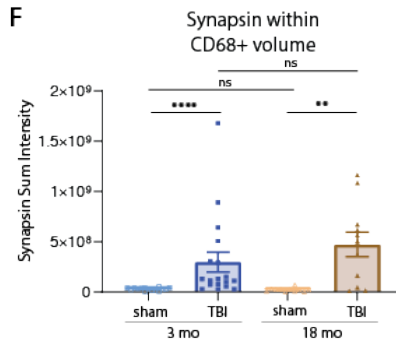
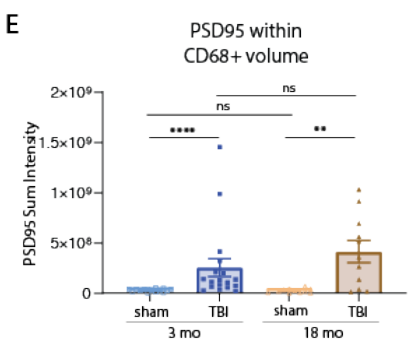
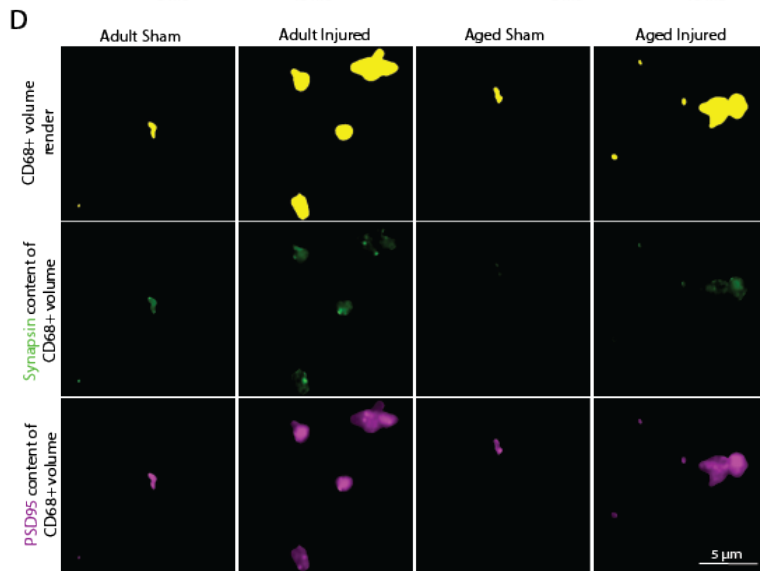
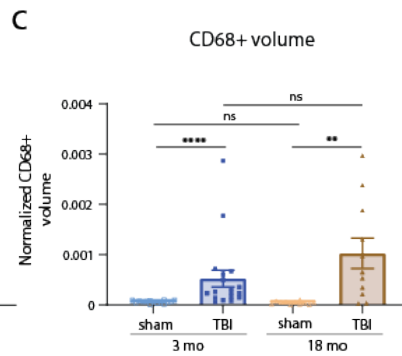
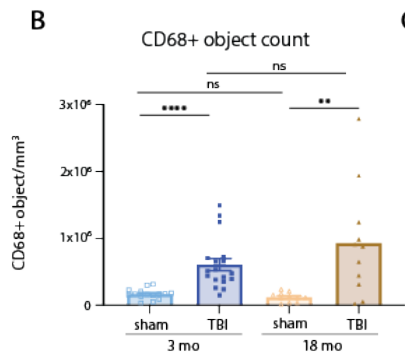
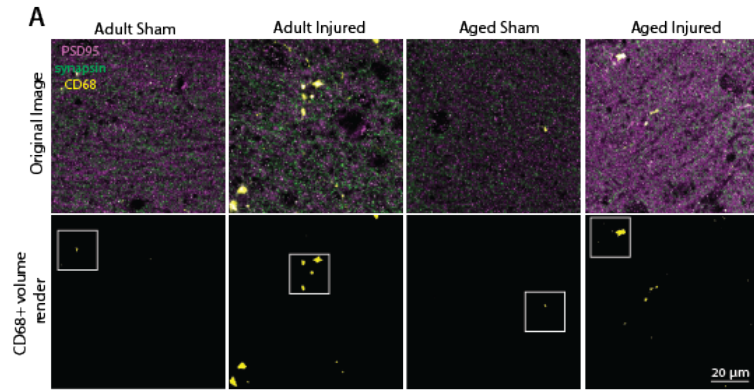


**Figure 4.4. TBI increases CD68+ volume.** A. Synaptic marker and CD68 labeling in hippocampal CA1. Imaging data is shown in the top row, the rendered CD68+ volume is illustrated in the second. B. Density of CD68+ objects per field. C. CD68+ volume normalized to image volume. D. CD68+ volume render (top row) with synapsin (middle) and PSD95 (bottom) labeling within the rendered CD68+ volume. E-F. Quantification of total PSD95 (E) and synapsin (F) labeling within CD68+ volume. \*\* $p < 0.01$ , \*\*\*\* $p < 0.0001$

### 4.3.5 Functional Outcomes

To investigate potential age-related functional disparities following TBI, Morris Water Maze performance was analyzed. On day 5 of the water maze spatial learning paradigm, adult and aged sham-injured animals demonstrated significantly improved spatial navigation compared to their first day of training as measured by average distance to the platform across four trials (adult sham day 1 mean=844.1, adult sham day 5 mean=319.3, Cohen's  $D=2.14$ ; aged sham day 1 mean=699.4, aged sham day 5 mean=327.5, Cohen's  $D=2.75$ ) (figure 4.5 A-C). Adult and aged animals subjected to TBI, however, did not show substantial learning between days (adult TBI day 1 mean=772.4, adult TBI day 5 mean=609.8, Cohen's  $D=0.74$ ; aged TBI day 1 mean=863.6, aged TBI day 5 mean=680.7, Cohen's  $D=1.09$ ). Direct comparison on day 5 also revealed shorter distances to target among the sham-injured animals (at both age ranges) than in animals that underwent TBI (adult Cohen's  $D=1.61$ ; aged Cohen's  $D=2.29$ ). However, age at injury did not significantly modify Morris Water Maze performance in sham-injured animals nor following TBI (sham Cohen's  $D=0.01$ , injured Cohen's  $D=0.36$ ). Animals were also tested in the Y maze, but performance (percent alternations) was effected by neither TBI nor age (adult sham mean=51.30, adult TBI mean=53.22, Cohen's  $D=0.24$ ; aged sham mean=55.28, aged TBI mean=56.87, Cohen's  $D=0.16$ ; effect of age in sham animals by Cohen's  $D=0.49$ ; effect of age in TBI animals by Cohen's  $D=0.39$ )(figure 4.5 D). Adult animals subjected to TBI were more exploratory in the Y maze as measured by number of arm entries, a trend also observed in aged

animals (adult sham mean=38.67, adult TBI mean=47.14, Cohen's  $D=0.85$ ; aged sham mean=27.87, aged TBI mean=34.71, Cohen's  $D=0.81$ )(figure 4.5 E). Adult animals were also more exploratory than aged animals irrespective of TBI status (sham Cohen's  $D=1.43$ ; TBI Cohen's  $D=1.17$ ). All groups, furthermore, displayed similar thigmotactic behavior in the open field test as measured by time-weighted distance from the wall(adult sham mean=5.52, adult TBI mean=5.54, Cohen's  $D=0.03$ ; aged sham mean=5.61, aged TBI mean=5.02, Cohen's  $D=1.05$ . However, adult injured animals again exhibited increased exploratory behavior compared to their sham-injured controls (adult sham mean=2416, adult TBI mean=3019, Cohen's  $D=1.24$ ), an effect not observed in aged animals (aged sham mean=2100, aged TBI mean=2234, Cohen's  $D=0.28$ ).

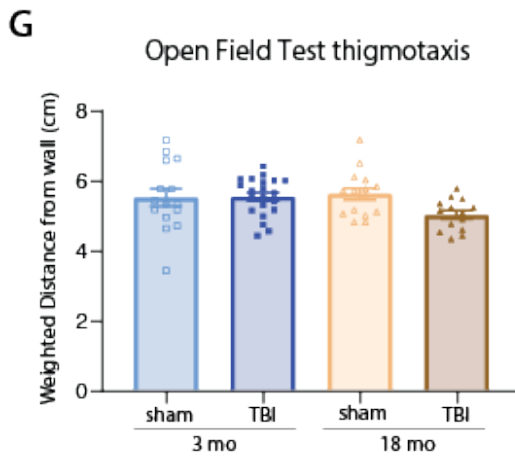
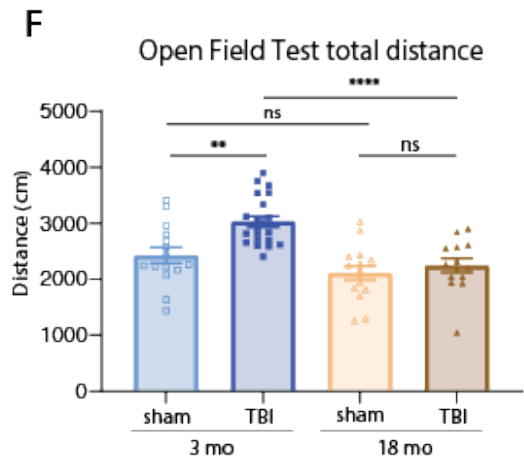
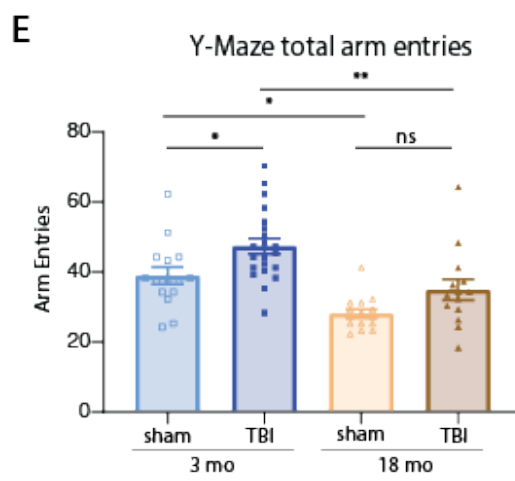
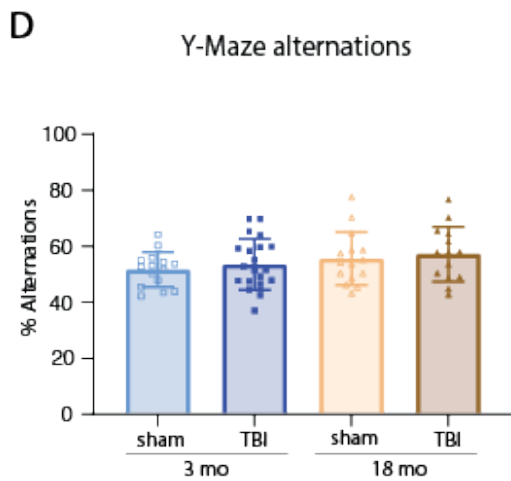
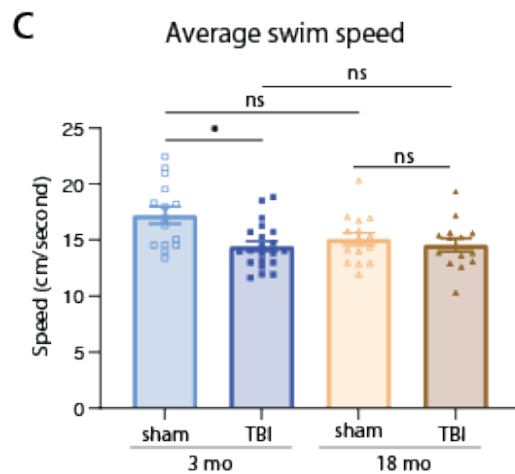
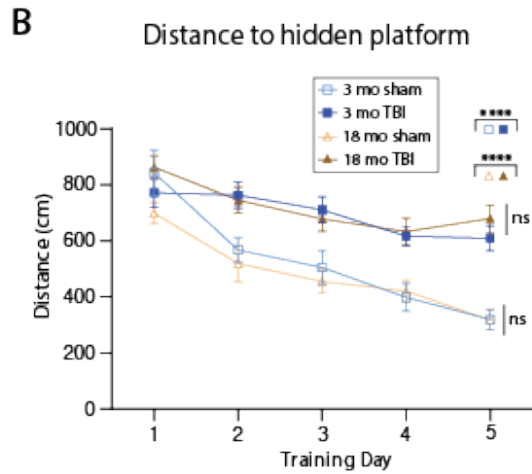
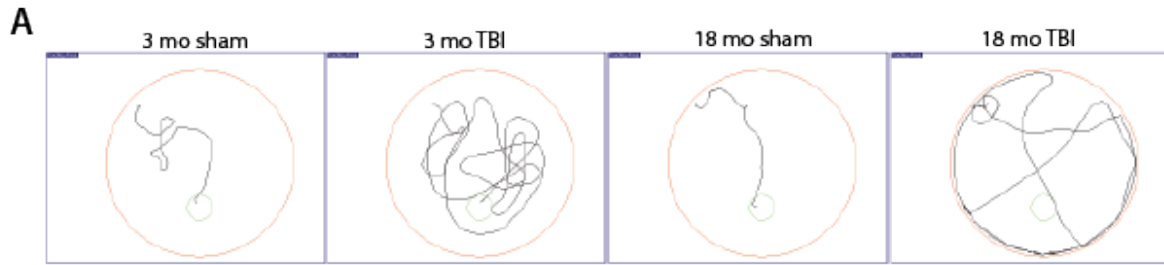


### **Figure 4.5. Minimal age-dependent effects on functional endpoints after TBI.**

A. Representative traces of animals from each group searching for the platform on day 5 of Morris Water Maze hidden platform testing. B. Distance to reach hidden platform across five days of Morris Water Maze training. C. Average swim speed on day 5 of Morris Water Maze hidden platform training. D. Total Y-maze arm entries. E. Number of alternations as a function of the total number of arm entry triplets. F. Thigmotaxic behavior in the open field test. G. Total distance traveled during the open field test. \* $p < 0.05$ , \*\* $p < 0.01$ , \*\*\*\* $p < 0.0001$

## **4.4 Discussion**

In summary, aged humans are both 1) more likely to suffer a TBI and 2) experience worse outcome than their younger peers (Annegers et al., 1998; Annegers and Coan, 2000; Centers for Disease Control, 2021; Green et al., 2008; Mosenthal et al., 2004; Stocchetti et al., 2012). However, mechanisms underpinning this disparity in outcome remain widely unexplored. This study sought to define differences in structure, neuroinflammation, and function following a moderate-to-severe experimental TBI in the hopes of shedding light on this question.

Examining structural endpoints, a significant loss of excitatory synapses of the CA1 molecular layer ipsilateral to the focal component of the injury following experimental TBI was demonstrated, but no effect of age in both sham-injured and TBI groups was detected. This lack of an effect of age on CA1 synapse loss is supported by previous literature demonstrating no age-dependent effect of CA1 synapse loss in the healthy aged brain, as compared to reports of age-dependent synapse loss in the dentate gyrus (Calhoun et al., 1998; Geinisman et al., 2004, 1992; Rapp and Gallagher, 1996). Additionally, loss of synapses following TBI in adult animals has been demonstrated across multiple models of injury, supporting this study's findings of injury-dependent synapse loss (Sauerbeck et al., 2020; Scheff et al., 2005).

This study found that both adult and aged animals subjected to TBI had a subgroup of animals containing large hippocampal lesions. This hippocampal lesion was more prevalent in aged TBI animals than adult TBI animals. While this difference in proportion of injured animals with a hippocampal lesion failed to reach statistical significance, this is likely due to small group sized of adult injured animals, and there is in fact a meaningful difference in presence of hippocampal lesion between adult and aged animals. This is supported findings that aged animals exhibiting larger lesion size following TBI than adult animals (Kumar et al., 2013).

When measuring nuclear band thickness in animals without frank disruption of the CA1 nuclear bands, no effect of injury was detected in adult or aged injured animals. However, a small decrease in nuclear band thickness was observed in aged sham-injured animals when compared to adult sham-injured animals, which is surprising given robust literature suggesting aging does not cause CA1 pyramidal cell loss in rodents, even in presence of age-related cognitive decline(Calhoun et al., 1998; Rapp and Gallagher, 1996). Differences in findings could be due to different quantification methods. Additionally, given the small effect size results, could have little-to-no biological significance.

To evaluate microgliosis, this study measured microglial density, proliferation, microglial endosome/lysosome volume, and microglial synaptic phagocytosis. While TBI significantly increased all endpoints at both ages, no effect of age was found in sham-injured animals, indicating inflammation is not increased by aging alone in the CA1 molecular layer of the hippocampus as measured by these endpoints. However, reports of both microglial density and endosome and lysosome volume changes in rodents as a function of aging are highly region specific(Long et al., 1998; Sharaf et al., 2013), indicating that it is possible the ROI used in this study did not capture all age-related changes in microgliosis in healthy aged animals. Turning to

animals subjected to TBI, while microglial density was the only endpoint significantly higher in aged animals compared to adult animals, all other endpoints trended higher in aged vs. adult animals. This suggests aged that aged animals have a higher neuroinflammatory profile at a subacute timepoint following injury compared to than animals. Overall, this study found that animals of both ages that received a TBI had significantly increased microgliosis in the CA1 molecular layer of the hippocampus. Furthermore, as both groups who underwent TBI displayed increased synaptic phagocytosis at a subacute timepoint compared to controls, as measured by PSD95 and synapsin content in lysosomes/endosomes, this suggests synaptic stripping is continuing well after the moment of injury. This is supported by my and my colleague's work showing synaptic density continues to decrease at least to 30 days following TBI in adult animals (Sauerbeck et al., 2020).

While increased age had no effect on learning and memory in either the sham-injured or TBI groups, TBI caused a substantial deficit at both ages. While literature suggests normal aging can cause deficits in rodent Morris Water Maze performance, aged animals often stratify into two groups: normal learners and impaired learners (Geinisman et al., 2004; Rapp and Gallagher, 1996) and other studies find no difference in performance between adult and aged animals (Calhoun et al., 1998). Furthermore, while a limited body of literature has shown worse functional outcome following TBI in an aged versus adult rodent population (Ritzel et al., 2019), which is supported by reports of worsened functional outcome in humans (Green et al., 2008; Hukkelhoven et al., 2003; Mosenthal et al., 2004; Stocchetti et al., 2012), this study was unable to detect a difference in learning and memory between adult and aged animals subjected to TBI. It is possible this is due to a ceiling effect. Alternatively, it is possible age at time of TBI does not impact spatial learning and memory.

The model of multimodal TBI employed in this study exhibited greater face validity TBI than using a focal or diffuse model of injury alone. However, this model yielded a focal lesion interrupting the CA1 nuclear band in 39% of adult animals and 75% of aged animals. This lesion limited hippocampal nuclear band quantification, hence limiting ability to correlate neuron loss to synaptic density and functional impairment. Future use of this model could limit CCI impact depth to produce an injury with a cortical lesion that does not directly damage the CA1 nuclear band and molecular layer.

Additionally, histopathological assessment was limited to the CA1 nuclear band and molecular layer. While this ROI was chosen due to both proximity to the lesion and its well-documented role in spatial learning and memory—key functional endpoints in this study—expanding the ROI could unveil further relationships between age and TBI.

# **Chapter 5: Conclusion and Future Directions**

## **5.1 Conclusions**

This thesis first describes technical developments and then employs them—among other techniques—to better understand relationship between age and brain injury.

The first technique described, SEQUIN (Chapter 2), utilizes super-resolution microscopy to achieve synaptic resolution(Reitz et al., 2021a; Sauerbeck et al., 2020), which allows for much higher throughput than techniques such as array tomography and electron microscopy due to straightforward tissue processing and high levels of imaging and image analysis automation.

The second technique described adds an additional channel to standard immunofluorescence microscopy using a long-Stokes shifted fluorophore, ATTO 490LS(ATTO-TEC GmbH, n.d.; Reitz et al., 2021b)(Chapter 3). This allows for two fluorophores (in this work, Alexa Fluor 488 and Atto 490LS) to be excited using the same laser but spectrally separated using different filter sets, as most antibodies have much smaller stokes shifts, or separation between the excitation and emission peak. The key benefit to this approach is that it adds a fourth, highly quantitative imaging channel with no spectral cross talk.

Finally, work presented in this thesis characterizes of the role of both age and TBI in hippocampal CA1 microstructure, microgliosis, and function using a model of focal and diffuse TBI and the above techniques (Chapter 4).

In sum, this thesis describes not only technical developments that can be applied both the field of brain injury and neuroscience as a whole, but utilizes these techniques to understand the role of age at TBI on histopathological and functional outcome.

## **5.1.1 Microstructural changes following TBI in the adult and aged mouse brain**

### **5.1.1.1 Synapse loss following TBI**

Synapse loss has been well-established as a consequence of TBI at varying timepoints post-injury. Gao et al. showed reduction in synaptic density in the dentate gyrus at 72 hours post-TBI in mice(Gao et al., 2011), and Scheff et al. showed decreased synaptic density in the CA1 region of the hippocampus at timepoints 2-60 days post-TBI in rats (Scheff et al., 2005). Additionally, loss of dendritic proteins in rodents following focal brain injury has been reported(Huh et al., 2003; Posmantur et al., 1996).

Given the high complexity of synaptic networks and small size of synapses, most synaptic quantification techniques capable of reaching synaptic resolution, such as array tomography and electron microscopy, require a high degree of technical expertise and are often quite time-consuming. We developed SEQUIN (Synaptic Evaluation and Quantification by Imaging Nanostructure) as a highly accessible, high throughput technique that reaches synaptic resolution by utilizing super resolution microscopy(Reitz et al., 2021a; Sauerbeck et al., 2020)(Chapter 2). By implementing SEQUIN we were able greatly increase tissue volume in which synapses were quantified and decrease active time acquiring images and performing quantification.

Furthermore, by developing a protocol for using a long-Stokes shifted fluorophore (Chapter 3), we were able to simultaneously label four synaptic proteins in the same section of tissue, and differentiate and quantify multiple synaptic subsets(Reitz et al., 2021b; Sauerbeck et al., 2020).

When applied to a diffuse model of TBI, SEQUIN has previously shown loss of cortical excitatory synaptic density, with synaptic density continuing to decrease until 30 days post-injury (Sauerbeck et al., 2020). This thesis describes synaptic quantification using SEQUIN in a

multimodal model of injury in both adult and aged animals 30 days post-injury. Synaptic density was measured in the ipsilateral CA1 molecular layer due both to this area's proximity to the lesion and salience to learning and memory, key behavioral endpoints. Primarily, we found a substantial effect of TBI in both adult and aged animals as compared to age-matched sham-injured animals. These findings are aligned with our and other publications of synaptic density loss following TBI(Gao et al., 2011; Scheff et al., 2005).

However, we found no effect of age in synaptic density in both sham and injured animals. Results in sham animals are supported by work from a multitude of groups finding no CA1 synaptic density loss as a result of normal aging(Calhoun et al., 1998; Geinisman et al., 2004; T. D. Smith et al., 2000). It is possible these results were limited by the ROI, as age-dependent synapse loss has been observed in the rodent dentate gyrus and CA3(Adams et al., 2010; Geinisman et al., 1992; T. D. Smith et al., 2000).

#### **5.1.1.2 Neuron loss following TBI**

In addition to synapse loss, TBI has been shown cause neuronal apoptosis in both humans and animal models(Akamatsu and Hanafy, 2020; Conti et al., 1998; Dressler et al., 2007; Fox et al., 1998; F. M. Smith et al., 2000). To quantify neuronal death following TBI, nuclear band thickness was measured in the CA1 molecular layer in adult and aged animals at 35 days post-injury.

However, the multimodal injury model generated a large hippocampal lesion in a subgroup of both adult and aged mice receiving TBI, which was prohibitive of nuclear band thickness quantification. While differences between the adult and aged groups in proportion of animals exhibiting this grade of injury did not reach statistical significance, this is likely due to small group size of aged, injured animals. This would suggest that aged animals exhibit larger lesion

volume than adult animals following the multimodal injury model, which is supported findings that aged animals exhibit larger lesion size than adult animals following other models of TBI (Kumar et al., 2013).

When measuring nuclear band thickness in animals without frank disruption of the CA1 nuclear bands, no effect of injury was detected in adult or aged, injured animals. This contrasts human and animal model reports of neuronal apoptosis following TBI. One possible explanation is differing quantification techniques and ROIs examined. The referenced groups measured TUNEL-positive neurons in various regions of the brain not including the CA1 following injury as opposed this report's quantification of neurons by measuring CA1 nuclear band thickness post-injury (Akamatsu and Hanafy, 2020, 2020; Conti et al., 1998; Dressler et al., 2007; Fox et al., 1998; F. M. Smith et al., 2000).

A minor decrease in mean nuclear band thickness was observed in aged sham-injured animals as compared to adult sham-injured animals. This is unexpected due to robust literature suggesting aging does not cause CA1 pyramidal cell loss in rodents, even in presence of age-related cognitive decline (Calhoun et al., 1998; Rapp and Gallagher, 1996). Differences in findings could be attributed to different quantification methods, as these groups used stereo logical counting techniques while this report quantified neurons by measuring CA1 nuclear band thickness. Further, given the small effect, these findings could have little-to-no biological significance.

### **5.1.2 Neuroinflammatory profile changes following TBI in the adult and aged mouse brain**

Following TBI, the brain experiences a broad, long lasting change in neuroinflammatory profile. Quickly after initial insult, injured neurons release damage-associated molecular patterns (DAMPs), molecules that bind to pattern recognition receptors and instigate an immune

response, including activating microglia. Once activated, microglia, the resident immune cell of the brain, release an array of pro-inflammatory cytokines, excitatory neurotransmitters, and reactive oxygen species (ROS), propagating the inflammatory response. (Izzy et al., 2019; Smith et al., 2013). In adults who suffered TBI, the number of activated microglia is significantly greater than in age-matched controls even decades after injury (Johnson et al., 2013; Ramlackhansingh et al., 2011).

Interestingly, the healthy aged brain is known to exhibit some signs of neuroinflammation at baseline, including a higher proportion of activated microglia, increased expression of proinflammatory cytokines, and decreased expression of anti-inflammatory cytokines.

(Perry et al., 1993; Rozovsky et al., 1998; Sandhir et al., 2008; Sheffield and Berman, 1998). To evaluate differences in neuroinflammatory profile following TBI between adult and aged animals, we evaluated microglial density, proliferation, endo-lysosomal volume, and synaptic phagocytosis in the CA1 molecular layer of the hippocampus.

This is the first study to describe synaptic phagocytosis by microglia following TBI. To do so, tissue was labeled with four antigens targeting microglia (Iba1), endosomes and lysosomes (CD68), and pre- and postsynaptic proteins (synapsin and PSD95). To achieve this four antigen labeling and visualization, the long-Stokes shifted antibody described in Chapter 3 was employed (Reitz et al., 2021b). It was then confirmed that CD68 was only found in microglia, and PSD95 and synapsin fluorescence from inside the CD68+ objects were quantified.

Overall, TBI significantly increased microgliosis at both ages for prolonged periods. This work found significant changes between sham-injured and TBI mice of both age groups in the domains of microglial density, microglial proliferation at both acute and subacute timepoints, endo-

lysosomal volume as measured by CD68, and synaptic phagocytosis. Additionally, as both adult and aged animals displayed increased synaptic phagocytosis at a 35 days following a TBI, as compared sham-injured age-matched controls, this suggests synaptic stripping is continuing well after the moment of injury. This is supported by my and my colleague's work showing synaptic density continues to decrease at least to 30 days following TBI in adult animals (Sauerbeck et al., 2020).

However, no effect of age was found in sham-injured animals across any neuroinflammatory domain. This indicates neuroinflammation is not increased by aging alone in the CA1 molecular layer of the hippocampus as measured by these endpoints. As reports of both microglial density and endosome and lysosome volume changes in rodents as a function of aging take place using cultured microglia and this report's quantifications are performed in situ, it is likely the disparity in results is due to different techniques(Henry et al., 2009; Rozovsky et al., 1998). This is supported by findings from other groups who report no change in microglial density between adult and aged animals (Hefendehl et al., 2014; Long et al., 1998).

When measuring neuroinflammation in animals who underwent TBI, microglial density was significantly higher in aged animals compared to adult animals, which is supported by previous studies showing increased neuroinflammation following TBI in aged versus adult animals(Kumar et al., 2013). In addition, while not reach statistical significance, microglial proliferation at both acute and subacute timepoints trended higher in aged animals as compared to adult animals following TBI. In sum, these findings suggest that aged animals have a higher neuroinflammatory profile at a subacute timepoint following injury compared to adult animals.

### **5.1.3 Functional changes following TBI in the adult and aged brain**

TBI can cause a wide array of cognitive and behavioral changes in humans, relating both to severity of injury and location in the brain. Some of the most common behavioral effects of TBI include learning and memory impairment, and impaired judgment (Centers for Disease Control, 2015).

To measure learning and memory in adult and aged mice, the Morris Water Maze (Chapter 4) was employed and showed that TBI caused substantial learning and memory impairment in both ages. However, increased age did not impact learning and memory in either sham-injured or TBI groups. Regarding aged sham-injured animals, while literature suggests normal aging can cause deficits in rodent Morris Water Maze performance, aged animals often stratify into two groups: normal learners and impaired learners (Geinisman et al., 2004; Rapp and Gallagher, 1996) and other studies find no difference in performance between adult and aged animals (Calhoun et al., 1998).

Furthermore, while a limited body of literature has shown worse functional outcome following TBI in an aged versus adult rodent population (Ritzel et al., 2019), which is supported by reports of worsened functional outcome in humans (Green et al., 2008; Hukkelhoven et al., 2003; Mosenthal et al., 2004; Stocchetti et al., 2012), this study was unable to detect a difference in learning and memory between adult and aged animals subjected to TBI. This could be due to a ceiling effect. Alternatively, it is possible age at time of TBI does not impact spatial learning and memory in this system.

When correlating functional outcome as measured by distance to reach the platform on the fifth day of Morris Water Maze, no correlations reached statistical significance. However, a consistent, positive relationship between microglial number and distance to platform was

observed, and a consistent, negative relationship between synapses and distance to platform, indicating increased neuroinflammation and decreased synaptic density are related to poorer learning and memory.

#### **5.1.4 Summary**

In closing, this thesis developed and employed novel techniques to characterize microstructural changes and detect differences in neuroinflammation. Histological data was then compared to behavioral data to explore the relationship between pathology and functional deficits. Overall, this demonstrated profound synapse loss and learning and memory impairment, and a prolonged increase in microgliosis present in the CA1 molecular layer following TBI in both adult and aged animals. While no measurable differences between adult and aged sham-injured animals was detected outside of a small decrease in neuron band thickness, this thesis found that aged TBI-injured animals had increased microgliosis as compared to adult TBI-injured animals. In combination, these results show that TBI causes a prolonged increase in neuroinflammatory profile that may be differentially regulated in adult and aged animals.

## **5.2 Future Directions**

This work's finding of increased microgliosis in both adult and aged animals at a subacute timepoint following TBI sets the stage for several interesting future studies. Primarily, given the findings of increased microgliosis in aged animals compared to adult animals following TBI, a timecourse of neuroinflammation reduction should be established in both ages to illuminate age-driven differences. To do this, collection of key histological data such as CD68 immunoreactivity and Iba<sup>+</sup> cell morphology would be assessed at various timepoints following TBI. To increase robustness of results, one would then assess changes in expression of pro-inflammatory genes such as TNF- $\alpha$  and IL1 $\beta$  and *anti*-inflammatory genes such as IL-10 and

TGF $\beta$ . Any differences between adult and aged animals' rate of inflammation reduction following injury should then be thoroughly explored in post-mortem human tissue as a potential mechanism of outcome disparity.

Additionally, to describe differences in the role of microgliosis in adult and aged animal pathology, microglial neuroinflammation could be blocked using a compound such as a colony stimulating factor 1 receptor (CSF1R) inhibitor. Administration of CSF1R inhibitors are known to eliminate ~95% of microglia from the brain(Henry et al., 2020; Willis et al., 2020) and then, when administration is ceased, microglia repopulate in the resting anti-inflammatory state(Elmore et al., 2014). Via depletion and repopulation, these compounds have demonstrated a rescue of both behavioral impairment and histopathology following experimental TBI(Henry et al., 2020; Willis et al., 2020) by restoring microglia to an anti-inflammatory state following injury. By comparing the effects of CSF1R inhibition-based microglial elimination and repopulation in adult and aged animals in the context of TBI, one could more thoroughly delineate the relationship between age and microgliosis following brain injury. For example, if one found that microglial repopulation rescued behavioral impairment in adult animals but not aged animals, this would suggest differential processes regulate outcome following TBI in aged animals.

Finally, this thesis explored the role of age at time of TBI on histopathological and functional outcome. Future studies could test the role of aging *with* a TBI on histopathological and functional outcome. Recent literature has highlighted the role of repeated mild-to-moderate TBI in athletes leading to dementia later in life, a phenomenon known as Chronic Traumatic

Encephalopathy(Gavett et al., 2011; McKee et al., 2009; Roberts et al., 1990). However, while TBI is known to be the primary environmental risk factor of Alzheimer's disease (Chauhan, 2014; Plassman et al., 2000), and human and animal studies both show increased neuroinflammation at semi-chronic to chronic timepoints post-injury(Kumar et al., 2015; Loane et al., 2014; Ramlackhansingh et al., 2011), the behavioral and histopathological changes through the lifespan following a single moderate-to-severe TBI have not been robustly demonstrated. To do this, one would injure animals as adults and age them to a chronic timepoint and compare both behavioral and histopathological outcome with age-matched sham animals. One would also want to evaluate differentially expressed genes. Histopathological differences and differences in gene expression could both increase understanding of and provide critical therapeutic targets for dementias following brain injury.

## References

- Adams, M.M., Donohue, H.S., Linville, M.C., Iversen, E.A., Newton, I.G., Brunso-Bechtold, J.K., 2010. Age-Related Synapse Loss In Hippocampal CA3 Is Not Reversed By Caloric Restriction. *Neuroscience* 171, 373–382. <https://doi.org/10.1016/j.neuroscience.2010.09.022>
- Akamatsu, Y., Hanafy, K.A., 2020. Cell Death and Recovery in Traumatic Brain Injury. *Neurotherapeutics* 17, 446–456. <https://doi.org/10.1007/s13311-020-00840-7>
- Annegers, J.F., Coan, S.P., 2000. The risks of epilepsy after traumatic brain injury. *Seizure* 9, 453–457. <https://doi.org/10.1053/seiz.2000.0458>
- Annegers, J.F., Hauser, W.A., Coan, S.P., Rocca, W.A., 1998. A Population-Based Study of Seizures after Traumatic Brain Injuries. *N Engl J Med* 338, 20–24. <https://doi.org/10.1056/NEJM199801013380104>
- ATTO-TEC GmbH, n.d. . ATTO 490LS. URL <https://www.atto-tec.com/product-141-142.html?language=en>
- Bottiroli, G.F., Croce, A.C., Locatelli, D., Nano, R., Giombelli, E., Messina, A., Benericetti, E., 1998. Autofluorescence of normal and neoplastic human brain tissue: an aid for intraoperative delineation of tumor resection margins, in: Foth, H.-J., Marchesini, R., Podbielska, H., Katzir, A. (Eds.), . Presented at the BiOS Europe '97, San Remo, Italy, pp. 183–191. <https://doi.org/10.1117/12.297933>
- Brody, D.L., Mac Donald, C., Kessens, C.C., Yuede, C., Parsadonian, M., Spinner, M., Kim, E., Schwetye, K.E., Holtzman, D.M., Bayly, P.V., 2007. Electromagnetic Controlled Cortical Impact Device for Precise, Graded Experimental Traumatic Brain Injury. *Journal of Neurotrauma* 24, 657–673. <https://doi.org/10.1089/neu.2006.0011>
- Calhoun, M.E., Kurth, D., Phinney, A.L., Long, J.M., Hengemihle, J., Mouton, P.R., Ingram, D.K., Jucker, M., 1998. Hippocampal neuron and synaptophysin-positive bouton number in aging C57BL/6 mice. *Neurobiol Aging* 19, 599–606. [https://doi.org/10.1016/s0197-4580\(98\)00098-0](https://doi.org/10.1016/s0197-4580(98)00098-0)
- Centers for Disease Control, 2021. Surveillance Report of Traumatic Brain Injury-related Hospitalizations and Deaths by Age Group, Sex, and Mechanism of Injury—United States, 2016 and 2017.

- Centers for Disease Control, 2019. TBI Data and Statistics. URL <https://www.cdc.gov/traumaticbraininjury/data/index.html> (accessed 10.13.20).
- Centers for Disease Control, 1999. Traumatic brain injury in the United States: A report to Congress. URL [https://www.cdc.gov/traumaticbraininjury/pdf/TBI\\_in\\_the\\_US.pdf](https://www.cdc.gov/traumaticbraininjury/pdf/TBI_in_the_US.pdf) (accessed 10.13.20).
- Chauhan, N.B., 2014. Chronic neurodegenerative consequences of traumatic brain injury. *Restor Neurol Neurosci* 32, 337–365. <https://doi.org/10.3233/RNN-130354>
- Conti, A.C., Raghupathi, R., Trojanowski, J.Q., McIntosh, T.K., 1998. Experimental Brain Injury Induces Regionally Distinct Apoptosis during the Acute and Delayed Post-Traumatic Period. *J Neurosci* 18, 5663–5672. <https://doi.org/10.1523/JNEUROSCI.18-15-05663.1998>
- Coons, A.H., Creech, H.J., Jones, R.N., Berliner, E., 1942. The Demonstration of Pneumococcal Antigen in Tissues by the Use of Fluorescent Antibody. *The Journal of Immunology* 45, 159–170. <https://doi.org/10.4049/jimmunol.45.3.159>
- DeKosky, S.T., Scheff, S.W., 1990. Synapse loss in frontal cortex biopsies in Alzheimer's disease: Correlation with cognitive severity. *Ann Neurol*. 27, 457–464. <https://doi.org/10.1002/ana.410270502>
- Dong, C., Madar, A.D., Sheffield, M.E.J., 2021. Distinct place cell dynamics in CA1 and CA3 encode experience in new environments. *Nat Commun* 12, 2977. <https://doi.org/10.1038/s41467-021-23260-3>
- Dressler, J., Hanisch, U., Kuhlisch, E., Geiger, K.D., 2007. Neuronal and glial apoptosis in human traumatic brain injury. *Int J Legal Med* 121, 365–375. <https://doi.org/10.1007/s00414-006-0126-6>
- Elmore, M.R.P., Najafi, A.R., Koike, M.A., Dagher, N.N., Spangenberg, E.E., Rice, R.A., Kitazawa, M., Matusow, B., Nguyen, H., West, B.L., Green, K.N., 2014. Colony-stimulating Factor 1 Receptor Signaling Is Necessary for Microglia Viability, Unmasking a Microglia Progenitor Cell in the Adult Brain. *Neuron* 82, 380–397. <https://doi.org/10.1016/j.neuron.2014.02.040>
- Fleiss, B., Gressens, P., 2012. Tertiary mechanisms of brain damage: a new hope for treatment of cerebral palsy? *The Lancet Neurology* 11, 556–566. [https://doi.org/10.1016/S1474-4422\(12\)70058-3](https://doi.org/10.1016/S1474-4422(12)70058-3)

Fluorescence SpectraViewer, n.d. URL [www.thermofisher.com/us/en/home/life-science/cell-analysis/labeling-chemistry/fluorescence-spectraviewer.html](http://www.thermofisher.com/us/en/home/life-science/cell-analysis/labeling-chemistry/fluorescence-spectraviewer.html)

Fox, G.B., Fan, L., Levasseur, R.A., Faden, A.I., 1998. Sustained Sensory/Motor and Cognitive Deficits With Neuronal Apoptosis Following Controlled Cortical Impact Brain Injury in the Mouse. *Journal of Neurotrauma* 15, 599–614. <https://doi.org/10.1089/neu.1998.15.599>

Friess, S.H., Lapidus, J.B., Brody, D.L., 2015. Decompressive Craniectomy Reduces White Matter Injury after Controlled Cortical Impact in Mice. *Journal of Neurotrauma* 32, 791–800. <https://doi.org/10.1089/neu.2014.3564>

Ganz, T., Fainstein, N., Elad, A., Lachish, M., Goldfarb, S., Einstein, O., Ben-Hur, T., 2022. Microbial pathogens induce neurodegeneration in Alzheimer’s disease mice: protection by microglial regulation. *Journal of Neuroinflammation* 19, 5. <https://doi.org/10.1186/s12974-021-02369-8>

Gao, X., Deng, P., Xu, Z.C., Chen, J., 2011. Moderate traumatic brain injury causes acute dendritic and synaptic degeneration in the hippocampal dentate gyrus. *PLoS One* 6, e24566. <https://doi.org/10.1371/journal.pone.0024566>

Gavett, B.E., Stern, R.A., McKee, A.C., 2011. Chronic Traumatic Encephalopathy: A Potential Late Effect of Sport-Related Concussive and Subconcussive Head Trauma. *Clinics in Sports Medicine* 30, 179–188. <https://doi.org/10.1016/j.csm.2010.09.007>

Geinisman, Y., deToledo-Morrell, L., Morrell, F., Persina, I.S., Rossi, M., 1992. Age-related loss of axospinous synapses formed by two afferent systems in the rat dentate gyrus as revealed by the unbiased stereological dissector technique. *Hippocampus* 2, 437–444. <https://doi.org/10.1002/hipo.450020411>

Geinisman, Y., Ganeshina, O., Yoshida, R., Berry, R.W., Disterhoft, J.F., Gallagher, M., 2004. Aging, spatial learning, and total synapse number in the rat CA1 stratum radiatum. *Neurobiol Aging* 25, 407–416. <https://doi.org/10.1016/j.neurobiolaging.2003.12.001>

Green, R.E., Colella, B., Christensen, B., Johns, K., Frasca, D., Bayley, M., Monette, G., 2008. Examining Moderators of Cognitive Recovery Trajectories After Moderate to Severe Traumatic Brain Injury. *Archives of Physical Medicine and Rehabilitation* 89, S16–S24. <https://doi.org/10.1016/j.apmr.2008.09.551>

- Hammell, C.L., Henning, J.D., 2009. Prehospital management of severe traumatic brain injury. *BMJ* 338, b1683–b1683. <https://doi.org/10.1136/bmj.b1683>
- Hefendehl, J.K., Neher, J.J., Sühs, R.B., Kohsaka, S., Skodras, A., Jucker, M., 2014. Homeostatic and injury-induced microglia behavior in the aging brain. *Aging Cell* 13, 60–69. <https://doi.org/10.1111/acer.12149>
- Henry, C.J., Huang, Y., Wynne, A.M., Godbout, J.P., 2009. Peripheral lipopolysaccharide (LPS) challenge promotes microglial hyperactivity in aged mice that is associated with exaggerated induction of both pro-inflammatory IL-1 $\beta$  and anti-inflammatory IL-10 cytokines. *Brain, Behavior, and Immunity* 23, 309–317. <https://doi.org/10.1016/j.bbi.2008.09.002>
- Henry, R.J., Ritzel, R.J., Barrett, J.P., Doran, S.J., Jiao, Y., Leach, J.B., Szeto, G.L., Wu, J., Stoica, B.A., Faden, A.I., Loane, D.J., 2020. Microglial Depletion with CSF1R Inhibitor During Chronic Phase of Experimental Traumatic Brain Injury Reduces Neurodegeneration and Neurological Deficits. *J Neuroscience* 40, 2960–2974. <https://doi.org/10.1523/JNEUROSCI.2402-19.2020>
- Henstridge, C.M., Pickett, E., Spires-Jones, T.L., 2016. Synaptic pathology: A shared mechanism in neurological disease. *Ageing Res Rev* 28, 72–84. <https://doi.org/10.1016/j.arr.2016.04.005>
- Huh, J.W., Raghupathi, R., Laurer, H.L., Helfaer, M.A., Saatman, K.E., 2003. Transient Loss of Microtubule-Associated Protein 2 Immunoreactivity after Moderate Brain Injury in Mice. *Journal of Neurotrauma* 20, 975–984. <https://doi.org/10.1089/089771503770195821>
- Hukkelhoven, C.W.P.M., Steyerberg, E.W., Rampen, A.J.J., Farace, E., Habbema, J.D.F., Marshall, L.F., Murray, G.D., Maas, A.I.R., 2003. Patient age and outcome following severe traumatic brain injury: an analysis of 5600 patients. *Journal of Neurosurgery* 99, 666–673. <https://doi.org/10.3171/jns.2003.99.4.0666>
- Izzy, S., Liu, Q., Fang, Z., Lule, S., Wu, L., Chung, J.Y., Sarro-Schwartz, A., Brown-Whalen, A., Perner, C., Hickman, S.E., Kaplan, D.L., Patsopoulos, N.A., El Khoury, J., Whalen, M.J., 2019. Time-Dependent Changes in Microglia Transcriptional Networks Following Traumatic Brain Injury. *Front. Cell. Neurosci.* 13, 307. <https://doi.org/10.3389/fncel.2019.00307>

- Jaiswal, J.K., Simon, S.M., 2004. Potentials and pitfalls of fluorescent quantum dots for biological imaging. *Trends Cell Biol* 14, 497–504. <https://doi.org/10.1016/j.tcb.2004.07.012>
- Johnson, V.E., Stewart, J.E., Begbie, F.D., Trojanowski, J.Q., Smith, D.H., Stewart, W., 2013. Inflammation and white matter degeneration persist for years after a single traumatic brain injury. *Brain* 136, 28–42. <https://doi.org/10.1093/brain/aws322>
- Kumar, A., Stoica, B.A., Sabirzhanov, B., Burns, M.P., Faden, A.I., Loane, D.J., 2013. Traumatic brain injury in aged animals increases lesion size and chronically alters microglial/macrophage classical and alternative activation states. *Neurobiology of Aging* 34, 1397–1411. <https://doi.org/10.1016/j.neurobiolaging.2012.11.013>
- Kumar, R.G., Boles, J.A., Wagner, A.K., 2015. Chronic Inflammation After Severe Traumatic Brain Injury: Characterization and Associations With Outcome at 6 and 12 Months Postinjury. *The Journal of Head Trauma Rehabilitation* 30, 369. <https://doi.org/10.1097/HTR.0000000000000067>
- Loane, D.J., Kumar, A., Stoica, B.A., Cabatbat, R., Faden, A.I., 2014. Progressive Neurodegeneration After Experimental Brain Trauma: Association With Chronic Microglial Activation. *Journal of Neuropathology & Experimental Neurology* 73, 14–29. <https://doi.org/10.1097/NEN.0000000000000021>
- Long, J.M., Kalehua, A.N., Muth, N.J., Calhoun, M.E., Jucker, M., Hengemihle, J.M., Ingram, D.K., Mouton, P.R., 1998. Stereological analysis of astrocyte and microglia in aging mouse hippocampus. *Neurobiol Aging* 19, 497–503. [https://doi.org/10.1016/s0197-4580\(98\)00088-8](https://doi.org/10.1016/s0197-4580(98)00088-8)
- Marr, A.L., Coronado, V., 2004. Central nervous system injury surveillance data submission standards. US Department of Health and Human Services, CDC.
- Masel, B.E., DeWitt, D.S., 2010. Traumatic Brain Injury: A Disease Process, Not an Event. *Journal of Neurotrauma* 27, 1529–1540. <https://doi.org/10.1089/neu.2010.1358>
- Matuskey, D., Tinaz, S., Wilcox, K.C., Naganawa, M., Toyonaga, T., Dias, M., Henry, S., Pittman, B., Ropchan, J., Nabulsi, N., Suridjan, I., Comley, R.A., Huang, Y., Finnema, S.J., Carson, R.E., 2020. Synaptic Changes in Parkinson Disease Assessed with in vivo Imaging. *Ann Neurol* 87, 329–338. <https://doi.org/10.1002/ana.25682>

- McKee, A.C., Cantu, R.C., Nowinski, C.J., Hedley-Whyte, E.T., Gavett, B.E., Budson, A.E., Santini, V.E., Lee, H.-S., Kubilus, C.A., Stern, R.A., 2009. Chronic Traumatic Encephalopathy in Athletes: Progressive Tauopathy following Repetitive Head Injury. *J Neuropathol Exp Neurol* 68, 709–735. <https://doi.org/10.1097/NEN.0b013e3181a9d503>
- McKee, A.C., Daneshvar, D.H., 2015. The neuropathology of traumatic brain injury, in: *Handbook of Clinical Neurology*. Elsevier, pp. 45–66. <https://doi.org/10.1016/B978-0-444-52892-6.00004-0>
- McRae, T.D., Oleksyn, D., Miller, J., Gao, Y.-R., 2019. Robust blind spectral unmixing for fluorescence microscopy using unsupervised learning. *PLoS One* 14, e0225410. <https://doi.org/10.1371/journal.pone.0225410>
- Mosenthal, A.C., Livingston, D.H., Lavery, R.F., Knudson, M.M., Lee, S., Morabito, D., Manley, G.T., Nathens, A., Jurkovich, G., Hoyt, D.B., Coimbra, R., 2004. The Effect of Age on Functional Outcome in Mild Traumatic Brain Injury: 6-Month Report of a Prospective Multicenter Trial: *The Journal of Trauma: Injury, Infection, and Critical Care* 56, 1042–1048. <https://doi.org/10.1097/01.TA.0000127767.83267.33>
- Murmu, R.P., Li, W., Szepesi, Z., Li, J.-Y., 2015. Altered Sensory Experience Exacerbates Stable Dendritic Spine and Synapse Loss in a Mouse Model of Huntington’s Disease. *Journal of Neuroscience* 35, 287–298. <https://doi.org/10.1523/JNEUROSCI.0244-14.2015>
- Mustafa, A.G., Alshboul, O.A., 2013. Pathophysiology of traumatic brain injury. *Neurosciences (Riyadh)* 18, 222–234.
- Neher, R.A., Mitkovski, M., Kirchhoff, F., Neher, E., Theis, F.J., Zeug, A., 2009. Blind source separation techniques for the decomposition of multiply labeled fluorescence images. *Biophys J* 96, 3791–3800. <https://doi.org/10.1016/j.bpj.2008.10.068>
- O’Rourke, N.A., Weiler, N.C., Micheva, K.D., Smith, S.J., 2012. Deep molecular diversity of mammalian synapses: why it matters and how to measure it. *Nat Rev Neurosci* 13, 365–379. <https://doi.org/10.1038/nrn3170>
- Pascu, A., Romanitan, M.O., Delgado, J.-M., Danaila, L., Pascu, M.-L., 2009. Laser-induced autofluorescence measurements on brain tissues. *Anat Rec (Hoboken)* 292, 2013–2022. <https://doi.org/10.1002/ar.21034>
- Perry, V.H., Matyszak, M.K., Fearn, S., 1993. Altered antigen expression of microglia in the aged rodent CNS. *Glia* 7, 60–67. <https://doi.org/10.1002/glia.440070111>

- Peterson, A.B., Kegler, S.R., 2010. Deaths from fall-related traumatic brain injury—United States, 2008-2017. *MMWR Morb Moral Wkly Rep* 69, 225–30. <https://doi.org/10.15585.mmwr.mm6909a2>
- Plassman, B.L., Havlik, R.J., Steffens, D.C., Helms, M.J., Newman, T.N., Drosdick, D., Phillips, C., Gau, B.A., Welsh-Bohmer, K.A., Burke, J.R., Guralnik, J.M., Breitner, J.C., 2000. Documented head injury in early adulthood and risk of Alzheimer’s disease and other dementias. *Neurology* 55, 1158–1166. <https://doi.org/10.1212/wnl.55.8.1158>
- Posmantur, R.M., Kampfl, A., Taft, W.C., Bhattacharjee, M., Dixon, C.E., Bao, J., Hayes, R.L., 1996. Diminished microtubule-associated protein 2 (MAP2) immunoreactivity following cortical impact brain injury. *J Neurotrauma* 13, 125–137. <https://doi.org/10.1089/neu.1996.13.125>
- Prasetyo, E., 2020. The primary, secondary, tertiary brain injury. *Crit Care Shock* 23, 4–13.
- Ramlackhansingh, A.F., Brooks, D.J., Greenwood, R.J., Bose, S.K., Turkheimer, F.E., Kinnunen, K.M., Gentleman, S., Heckemann, R.A., Gunanayagam, K., Gelosa, G., Sharp, D.J., 2011. Inflammation after trauma: Microglial activation and traumatic brain injury. *Ann Neurol*. 70, 374–383. <https://doi.org/10.1002/ana.22455>
- Rapp, P.R., Gallagher, M., 1996. Preserved neuron number in the hippocampus of aged rats with spatial learning deficits. *Proc Natl Acad Sci U S A* 93, 9926–9930. <https://doi.org/10.1073/pnas.93.18.9926>
- Reitz, S.J., Sauerbeck, A.D., Kummer, T.T., 2021a. SEQUIN: An imaging and analysis platform for quantification and characterization of synaptic structures in mouse. *STAR Protocols* 2. <https://doi.org/10.1016/j.xpro.2020.100268>
- Reitz, S.J., Sauerbeck, A.D., Kummer, T.T., 2021b. Enhanced Multiplexing of Immunofluorescence Microscopy Using a Long-Stokes-Shift Fluorophore. *Current Protocols* 1, e214. <https://doi.org/10.1002/cpz1.214>
- Resch-Genger, U., Grabolle, M., Cavaliere-Jaricot, S., Nitschke, R., Nann, T., 2008. Quantum dots versus organic dyes as fluorescent labels. *Nat Methods* 5, 763–775. <https://doi.org/10.1038/nmeth.1248>

- Ritzel, R.M., Doran, S.J., Glaser, E.P., Meadows, V.E., Faden, A.I., Stoica, B.A., Loane, D.J., 2019. Old age increases microglial senescence, exacerbates secondary neuroinflammation, and worsens neurological outcomes after acute traumatic brain injury in mice. *Neurobiology of Aging* 77, 194–206. <https://doi.org/10.1016/j.neurobiolaging.2019.02.010>
- Roberts, G.W., Allsop, D., Bruton, C., 1990. The occult aftermath of boxing. *J Neurol Neurosurg Psychiatry* 53, 373–378. <https://doi.org/10.1136/jnnp.53.5.373>
- Rozovsky, I., Finch, C.E., Morgan, T.E., 1998. Age-Related Activation of Microglia and Astrocytes: In Vitro Studies Show Persistent Phenotypes of Aging, Increased Proliferation, and Resistance to Down-Regulation. *Neurobiology of Aging* 19, 97–103. [https://doi.org/10.1016/S0197-4580\(97\)00169-3](https://doi.org/10.1016/S0197-4580(97)00169-3)
- Sandhir, R., Onyszchuk, G., Berman, N.E.J., 2008. Exacerbated glial response in the aged mouse hippocampus following controlled cortical impact injury. *Experimental Neurology* 213, 372–380. <https://doi.org/10.1016/j.expneurol.2008.06.013>
- Sauerbeck, A.D., Fanizzi, C., Kim, J.H., Gangolli, M., Bayly, P.V., Wellington, C.L., Brody, D.L., Kummer, T.T., 2018. modCHIMERA: a novel murine closed-head model of moderate traumatic brain injury. *Sci Rep* 8, 7677. <https://doi.org/10.1038/s41598-018-25737-6>
- Sauerbeck, A.D., Gangolli, M., Reitz, S.J., Salyards, M.H., Kim, S.H., Hemingway, C., Gratuze, M., Makkapati, T., Kerschensteiner, M., Holtzman, D.M., Brody, D.L., Kummer, T.T., 2020. SEQUIN Multiscale Imaging of Mammalian Central Synapses Reveals Loss of Synaptic Connectivity Resulting from Diffuse Traumatic Brain Injury. *Neuron* 107, 257–273.e5. <https://doi.org/10.1016/j.neuron.2020.04.012>
- Scheff, S.W., Price, D.A., Hicks, R.R., Baldwin, S.A., Robinson, S., Brackney, C., 2005. Synaptogenesis in the hippocampal CA1 field following traumatic brain injury. *J Neurotrauma* 22, 719–732. <https://doi.org/10.1089/neu.2005.22.719>
- Selkoe, D.J., 2002. Alzheimer's Disease Is a Synaptic Failure. *Science* 298, 789–791. <https://doi.org/10.1126/science.1074069>
- Sharaf, A., Kriegelstein, K., Spittau, B., 2013. Distribution of microglia in the postnatal murine nigrostriatal system. *Cell Tissue Res* 351, 373–382. <https://doi.org/10.1007/s00441-012-1537-y>

- Sheffield, L.G., Berman, N.E.J., 1998. Microglial Expression of MHC Class II Increases in Normal Aging of Nonhuman Primates. *Neurobiology of Aging* 19, 47–55.  
[https://doi.org/10.1016/S0197-4580\(97\)00168-1](https://doi.org/10.1016/S0197-4580(97)00168-1)
- Smith, C., Gentleman, S.M., Leclercq, P.D., Murray, L.S., Griffin, W.S.T., Graham, D.I., Nicoll, J.A.R., 2013. The neuroinflammatory response in humans after traumatic brain injury: Neuroinflammation after brain injury. *Neuropathol Appl Neurobiol* 39, 654–666.  
<https://doi.org/10.1111/nan.12008>
- Smith, F.M., Raghupathi, R., MacKinnon, M.-A., McIntosh, T.K., Saatman, K.E., Meaney, D.F., Graham, D.I., 2000. TUNEL-positive staining of surface contusions after fatal head injury in man. *Acta Neuropathol* 100, 537–545. <https://doi.org/10.1007/s004010000222>
- Smith, T.D., Adams, M.M., Gallagher, M., Morrison, J.H., Rapp, P.R., 2000. Circuit-Specific Alterations in Hippocampal Synaptophysin Immunoreactivity Predict Spatial Learning Impairment in Aged Rats. *J Neurosci* 20, 6587–6593.  
<https://doi.org/10.1523/JNEUROSCI.20-17-06587.2000>
- Stocchetti, N., Paternò, R., Citerio, G., Beretta, L., Colombo, A., 2012. Traumatic Brain Injury in an Aging Population. *Journal of Neurotrauma* 29, 1119–1125.  
<https://doi.org/10.1089/neu.2011.1995>
- Susman, M., DiRusso, S.M., Sullivan, T., Risucci, D., Nealon, P., Cuff, S., Haider, A., Benzil, D., 2002. Traumatic Brain Injury in the Elderly: Increased Mortality and Worse Functional Outcome At Discharge Despite Lower Injury Severity: *The Journal of Trauma: Injury, Infection, and Critical Care* 53, 219–224.  
<https://doi.org/10.1097/00005373-200208000-00004>
- Terry, R.D., Masliah, E., Salmon, D.P., Butters, N., DeTeresa, R., Hill, R., Hansen, L.A., Katzman, R., 1991. Physical basis of cognitive alterations in alzheimer's disease: Synapse loss is the major correlate of cognitive impairment. *Ann Neurol*. 30, 572–580.  
<https://doi.org/10.1002/ana.410300410>
- Tsien, J.Z., Huerta, P.T., Tonegawa, S., 1996. The Essential Role of Hippocampal CA1 NMDA Receptor-Dependent Synaptic Plasticity in Spatial Memory. *Cell* 87, 1327–1338.  
[https://doi.org/10.1016/S0092-8674\(00\)81827-9](https://doi.org/10.1016/S0092-8674(00)81827-9)

- Tsurui, H., Nishimura, H., Hattori, S., Hirose, S., Okumura, K., Shirai, T., 2000. Seven-color fluorescence imaging of tissue samples based on Fourier spectroscopy and singular value decomposition. *J Histochem Cytochem* 48, 653–662. <https://doi.org/10.1177/002215540004800509>
- Vella, M.A., Crandall, M.L., Patel, M.B., 2017. Acute Management of Traumatic Brain Injury. *Surg Clin North Am* 97, 1015–1030. <https://doi.org/10.1016/j.suc.2017.06.003>
- Wegner, K.D., Hildebrandt, N., 2015. Quantum dots: bright and versatile in vitro and in vivo fluorescence imaging biosensors. *Chem. Soc. Rev.* 44, 4792–4834. <https://doi.org/10.1039/C4CS00532E>
- Willis, E.F., MacDonald, K.P.A., Nguyen, Q.H., Garrido, A.L., Gillespie, E.R., Harley, S.B.R., Bartlett, P.F., Schroder, W.A., Yates, A.G., Anthony, D.C., Rose-John, S., Ruitenber, M.J., Vukovic, J., 2020. Repopulating Microglia Promote Brain Repair in an IL-6-Dependent Manner. *Cell* 180, 833-846.e16. <https://doi.org/10.1016/j.cell.2020.02.013>
- Zimmermann, T., 2005. Spectral imaging and linear unmixing in light microscopy. *Adv Biochem Eng Biotechnol* 95, 245–265. <https://doi.org/10.1007/b102216>